atmosphere

MDPI

Article

A Coupled CH_4, CO and CO_2 Simulation for Improved Chemical Source Modeling

Beata Bukosa [1,*], Jenny A. Fisher [2], Nicholas M. Deutscher [2] and Dylan B. A. Jones [3]

[1] National Institute of Water and Atmospheric Research, Wellington 6021, New Zealand
[2] Centre for Atmospheric Chemistry, School of Earth, Atmospheric and Life Sciences, Faculty of Science, Medicine and Health, University of Wollongong, Wollongong, NSW 2422, Australia
[3] Department of Physics, University of Toronto, Toronto, ON M5S 1A7, Canada
* Correspondence: beata.bukosa@niwa.co.nz

Abstract: Understanding greenhouse gas–climate processes and feedbacks is a fundamental step in understanding climate variability and its links to greenhouse gas fluxes. Chemical transport models are the primary tool for linking greenhouse gas fluxes to their atmospheric abundances. Hence, accurate simulations of greenhouse gases are essential. Here, we present a new simulation in the GEOS-Chem chemical transport model that couples the two main greenhouse gases—carbon dioxide (CO_2) and methane (CH_4)—along with the indirect greenhouse gas carbon monoxide (CO) based on their chemistry. Our updates include the online calculation of the chemical production of CO from CH_4 and the online production of CO_2 from CO, both of which were handled offline in the previous versions of these simulations. In the newly developed coupled (online) simulation, we used consistent hydroxyl radical (OH) fields for all aspects of the simulation, resolving biases introduced by inconsistent OH fields in the currently available uncoupled (offline) CH_4, CO and CO_2 simulations. We compare our coupled simulation with the existing v12.1.1 GEOS-Chem uncoupled simulations run the way they are currently being used by the community. We discuss differences between the uncoupled and coupled calculation of the chemical terms and compare our results with surface measurements from the NOAA Global Greenhouse Gas Reference Network (NOAA GGGRN), total column measurements from the Total Carbon Column Observing Network (TCCON) and aircraft measurements from the Atmospheric Tomography Mission (ATom). Relative to the standard uncoupled simulations, our coupled results suggest a stronger CO chemical production from CH_4, weaker production of CO_2 from CO and biases in the OH fields. However, we found a significantly stronger chemical production of CO_2 in tropical land regions, especially in the Amazon. The model–measurement differences point to underestimated biomass burning emissions and secondary production for CO. The new self-consistent coupled simulation opens new possibilities when identifying biases in CH_4, CO and CO_2 source and sink fields, as well as a better understanding of their interannual variability and co-variation.

Keywords: carbon dioxide; carbon monoxide; chemical production; modeling; GEOS-Chem; carbon cycle

Citation: Bukosa, B.; Fisher, J.A.; Deutscher, N.M.; Jones, D.B.A. A Coupled CH_4, CO and CO_2 Simulation for Improved Chemical Source Modeling. *Atmosphere* **2023**, *14*, 764. http://doi.org/10.3390/atmos14050764

Academic Editor: Daniel Viúdez-Moreiras

Received: 11 March 2023
Revised: 20 April 2023
Accepted: 20 April 2023
Published: 22 April 2023

1. Introduction

Accurate simulations of greenhouse gases are vital for climate predictions. Carbon dioxide (CO_2) and methane (CH_4) are the two main anthropogenic greenhouse gases and have a significant impact on our climate. Due to human activities, the atmospheric amounts of CO_2 and CH_4 have increased globally by 40% and 150%, respectively, since the industrial revolution [1]. Carbon monoxide (CO) is less abundant than CO_2 and CH_4; however, through its indirect effects on CH_4, ozone and CO_2, it can also have a climate impact [2]. Changes in the atmospheric amounts of these gases, driven by changes in their sources and sinks, largely control our future climate, but uncertainties about these processes and their budgets still remain [3–5]. All three carbon greenhouse gases are chemically dependent, and a change in one can affect the others.

In the GEOS-Chem model, each of these gases have their own stand-alone simulation, decoupled from one another. All three simulations are widely used for carbon gas flux inversion and source attribution [6–12]. Previous studies have emphasized the importance of the inclusion of the 3-D chemical production of CO_2 from the collective oxidation of CO, CH_4 and non-methane volatile organic compounds (NMVOCs) [13,14], but this chemical production, together with the secondary production of CO from CH_4, is handled offline in the stand-alone carbon gas simulations of the GEOS-Chem model [15–17]. Moreover, the chemical production and hydroxyl radical (OH) fields used by each of these individual simulations are calculated from different model versions (based on the model version in use when the stand-alone simulation was developed), introducing inconsistencies between the simulations. Here, we present a new simulation in GEOS-Chem that couples CH_4, CO and CO_2 with an online calculation of their chemical production using consistent and updated OH fields for a more accurate simulation of these gases.

The dominant loss process of CH_4, the second most important anthropogenic greenhouse gas, is through a reaction with OH:

$$CH_4 + OH \rightarrow CH_3 + H_2O \quad (1)$$

that eventually leads to the formation of CO after a series of intermediate steps [18]:

$$CHO + O_2 \rightarrow CO + HO_2 \quad (2)$$

Both CH_4 and CO have a common sink in the atmosphere through the reaction with OH. The role of CO in determining tropospheric OH indirectly affects the atmospheric burden of CH_4 [19]. Along with CH_4, it is one of the principal sinks of OH. Through the reaction with OH, CO can also lead to the chemical formation of CO_2 [13,14]:

$$CO + OH \rightarrow CO_2 + H \quad (3)$$

The oxidation of both primary CO, from direct anthropogenic and biomass burning emissions, and secondary CO, as an intermediate in the oxidation of CH_4 and NMVOCs, leads to the formation of CO_2. CO_2 can also be produced from the oxidation of carboxy–peroxy radical (RCO_3) and alkenoid ozonolysis (reaction of ethene with ozone; C_2H_4+O_3) [20], but this is thought to only be a minor contributor.

In regions that are not dominated by strong anthropogenic point emissions or biomass burning emissions, the major source of CO is CH_4 oxidation by OH through Reactions (1) and (2) and the intermediate reactions. Studies have found the yield of CO from CH_4 oxidation to range from 0.70–1 [4,21–26]. The CO chemical production from CH_4 is estimated to be 760–1086 Tg CO yr^{-1}, with CO also chemically produced from NMVOCs, with estimates of 320–820 Tg CO yr^{-1} [4,17,25,27–30]. The combined CO chemical production represents more than half of the total CO source.

The reaction of CO with OH radicals represents its largest sink, removing 2325–2630 Tg CO yr^{-1} [15,17,25,28,29,31]. The total chemical CO_2 source is estimated to be around 1.04–1.1 Pg *C* yr^{-1} [14,15], which is approximately 12% of the annual anthropogenic CO_2 source (9.4 Pg *C* yr^{-1}, averaged for 2008–2017) [32]. Around 90–94% of the CO_2 chemical production is from CO oxidation [20,33]. In contrast to the majority of the CO_2 sources that are emitted at the surface, CO_2 from the oxidation of CO is produced throughout the atmosphere. Although significant efforts have been made to constrain the total budgets of CO_2, CH_4 and CO, discrepancies in the chemical terms between studies suggest that these terms are still subject to uncertainties that can impact our understanding of the total budgets [4,14,15,17,30].

In this study, we introduced a new simulation in the GEOS-Chem model that couples the chemistry of CH_4, CO and CO_2. The coupling of the carbon greenhouse gases represents an important modeling improvement and capability when studying these gases [34,35]. With the new coupled GEOS-Chem carbon simulation, we eliminated the previous of-

fline handling of the chemical production terms and OH inconsistency between the three species [15–17], enabling us to have (i) better estimates of the chemical terms, (ii) consistent OH fields between species, and (iii) simultaneous and consistent simulations of CH_4, CO and CO_2 that can help when constraining their fluxes based on their covariation [10,36,37]. Moreover, the coupled simulation removes the need to run the individual simulations separately if interested in all three gases, and it requires fewer computational resources than running three independent simulations.

We first describe the method for the online calculation of the chemical production and the difference between the existing (uncoupled) and new (coupled) versions of these simulations (Section 2). We then compare the stand-alone simulations of all three gases, each run the way they are currently being used by the community, with the coupled simulation. For both versions, we analyze their annual budgets and the contribution of chemical production to the total amount of each gas (Sections 3.1 and 3.2) as well as their global spatial and vertical distribution (Sections 3.3 and 3.4). We validate the new coupled simulations against global surface flask measurements at sites that are part of the NOAA Global Greenhouse Gas Reference Network (NOAA GGGRN), column measurements from the Total Carbon Column Observing Network (TCCON) and aircraft in situ measurements from the Atmospheric Tomography Mission (ATom) (Section 3.5). Finally, we discuss a sensitivity simulation designed to test the impact of using inconsistent OH fields between the three uncoupled simulations, an issue that impacts the existing uncoupled simulations but is resolved in our new coupled simulation (Section 3.6).

2. Methods

2.1. Uncoupled Geos-Chem Carbon Gas Simulations

The uncoupled CH_4, CO and CO_2 simulations used here are based on version 12.1.1 of the GEOS-Chem 3-D global chemical transport model. The existing uncoupled simulations are described in Nassar et al. [15] and Nassar et al. [38] for CO_2, Wecht et al. [16] and Maasakkers et al. [39] for CH_4 and Fisher et al. [17] for CO. Each of these simulations are used routinely and independently for evaluating new emission inventories, estimating and resolving emissions, analyzing spatial and temporal changes of CH_4, CO and CO_2, source/sink attribution and inversion studies [6–12].

These simulations are decoupled from other gases and from one another; hence, they require input fields, including chemical production rates and OH losses. GEOS-Chem can also perform a full chemistry simulation, known as coupled aerosol–oxidant chemistry in the troposphere and stratosphere simulation. Of the three species, only CO is simulated online in the full chemistry simulation. CO_2 and CH_4 are not modeled as active species in the full chemistry, and their response to sources and sinks can only be modeled via the currently uncoupled simulations. The full chemistry simulation is required for the functionality of some of the stand-alone simulations because it provides input fields for those simulations. Various versions of the full chemistry simulation were run previously by the developers of each uncoupled simulation to archive the production rates and oxidant fields that are currently used in the carbon gas simulations (Table 1). Both the production and oxidant fields are computed using 3-D archives of monthly average values. All three carbon gas simulations are linear, and each includes a suite of tracers tagged by source type and/or region.

The equations below describe the changes in the emission, deposition, production and loss terms that occur within each grid box for the stand-alone CH_4, CO and CO_2 simulations. Note that advective transport fluxes between grid boxes (including between the troposphere and the stratosphere) are in addition to the terms described in each equation. The GEOS-Chem model dynamically calculates the tropopause height at every timestep and uses this information to assign each grid box to either the troposphere or the stratosphere. The simulated CH_4 in the troposphere is based on Equation (4):

$$\frac{d[CH_{4Trop}]}{dt} = E_{CH_4} - S_{CH_4} - k_{CH_4,OH}[OH][CH_4] - k_{CH_4,Cl}[Cl][CH_4] \quad (4)$$

where E_{CH_4} represents the surface emissions (gas, oil, coal, livestock, landfills, wastewater, biofuel, rice, biomass burning, wetlands, seeps, termites and other anthropogenic emissions; see Table S1), S_{CH_4} is the sink from soil absorption, [OH], [Cl] and [CH_4] are the atmospheric concentrations of OH, Cl and CH_4, and $k_{CH_4,OH}$ and $k_{CH_4,Cl}$ are the pressure- and temperature-dependent rate constants for oxidation of CH_4 by OH and Cl, respectively. While [CH_4] is calculated at each model timestep, in the uncoupled simulation, [OH] and [Cl] are provided as monthly mean values archived from a prior full chemistry simulation.

In the stratosphere, Equation (4) becomes:

$$\frac{d[CH_{4Strat}]}{dt} = E_{CH_4} - L(CH_4) \quad (5)$$

where $L(CH_4)$ represents the stratospheric CH_4 sink based on stratospheric CH_4 loss frequencies archived from the NASA Global Modeling Initiative model [40,41] as described by Murray et al. [42].

Simulated CO in the troposphere is based on Equation (6):

$$\frac{d[CO_{Trop}]}{dt} = E_{CO} + P(CO) - k_{CO}[OH][CO] \quad (6)$$

where E_{CO} represents the surface emissions (fossil fuel, biofuel and biomass burning), P(CO) accounts for the chemical production of CO from CH_4 and NMVOC oxidation and k_{CO} is the pressure- and temperature-dependent rate constant for oxidation of CO by OH from the Jet Propulsion Laboratory (JPL) data evaluation [43]. As in the CH_4 simulation, [OH] is provided as a monthly mean value archived from a prior full chemistry simulation.

The chemical production of CO (P(CO)) can be further separated into the production from CH_4 ($P(CO)_{CH_4}$) and the production from NMVOCs ($P(CO)_{NMVOC}$):

$$P(CO) = P(CO)_{CH_4} + P(CO)_{NMVOC} \quad (7)$$

The $P(CO)_{CH_4}$ and $P(CO)_{NMVOC}$ terms are monthly averaged archived fields that were obtained with the v9-01-03 GEOS-Chem 2° × 2.5° full chemistry simulation from the simulated monthly CO chemical production rates (P(CO)) as described by Fisher et al. [17]. In brief, the simulated P(CO) is split offline to the $P(CO)_{CH_4}$ and $P(CO)_{NMVOC}$ terms based on the CH_4 loss rates ($L(CH_4)$) that are also simulated and saved from a full chemistry simulation. A 100% CO yield from CH_4 is assumed; hence, the production of CO from CH_4 is equal to the CH_4 loss:

$$P(CO)_{CH_4} = L(CH_4) \quad (8)$$

The remaining $P(CO)_{NMVOC}$ contribution is then calculated as the difference between the total CO production and the production of CO from CH_4:

$$P(CO)_{NMVOC} = P(CO) - P(CO)_{CH_4} \quad (9)$$

Since the 100% yield may overestimate the production of CO from the oxidation of CH_4, the simulation caps the $P(CO)_{CH_4}$ to the total P(CO), where it is greater than P(CO) [17]. Hence, this assumption will retain consistency in the P(CO) terms between the full chemistry and uncoupled simulations.

In the v9-01-03 full chemistry simulation used to calculate the $L(CH_4)$ and $P(CO)_{CH_4}$ fields used by the uncoupled CO simulation [17], CH_4 mixing ratios were prescribed as fixed values. One annual value for each of four latitude bands (30–90° S, 0–30° S, 0–30° N, 30–90° N) was applied throughout the troposphere, defined as averages of surface observations from NOAA carbon cycle surface flasks.

Table 1. GEOS-Chem production (*P*) and loss (*L*) terms used for the uncoupled and coupled carbon gas simulations, along with the full chemistry model versions used to create the chemical terms and hydroxyl radical (*OH*) fields. The chemical terms are for the troposphere unless otherwise specified. Other source and sink fields are shown in Table S1.

	CH_4	CO	CO_2
Fields used by both uncoupled and coupled simulations			
Stratospheric L(CH_4)	Archived fields [1]	-	-
Stratospheric L(CO)	-	GMI [2]	-
Stratospheric P(CO)	-	GMI [2]	-
$P(CO)_{NMVOC}$	-	$P(CO)_{NMVOC}$ = P(CO) − $P(CO)_{CH_4}$	-
	-	archived, full chemistry v9-01-03 [3]	-
Fields used by uncoupled simulations only			
L(CH_4) [4]	online [5]	archived, full chemistry v9-01-03 [3]	-
Time resolution	Every model timestep, 20 min	Monthly mean, 2009–2011 average	-
$P(CO)_{CH_4}$	-	archived, $P(CO)_{CH_4}$ = Trop. L(CH_4)	-
Time resolution	-	Monthly mean, 2009–2011 average	-
L(CO) [4,6]	-	online, v9-01-03 [OH] [3]	archived, full chemistry v8-02-01 [7]
Time resolution	-	Every model timestep, 20 min	Monthly mean, 2004–2010
P(CO_2) [6]	-	-	archived, P(CO_2) = L(CO)
Time resolution	-	-	Monthly mean, 2004–2010
Fields used by coupled simulation only			
L(CH_4)	online, v9-01-03 [OH] [3,8]	-	-
Time resolution	Every model timestep, 20 min	-	-
$P(CO)_{CH_4}$	-	online, $P(CO)_{CH_4}$ = L(CH_4)	-
Time resolution	-	Every model timestep, 20 min	-
L(CO)	-	online, v9-01-03 [OH] [3]	-
Time resolution	-	Every model timestep, 20 min	-
P(CO_2) [9]	-	-	online, P(CO_2) = L(CO)
Time resolution	-		Every model timestep, 20 min

[1] Murray et al. [42], [2] NASA Global Modeling Initiative model, [3] Fisher et al. [17], [4] Note that, in the uncoupled simulations, there are two entities for L(CH_4) and L(CO) because there is a different treatment based on whether they are being used to calculate the concentration of the species itself or as a proxy for the production of another species, [5] Note that the public uncoupled CH_4 simulation uses v5-07-08 OH fields [44]; however, the uncoupled CH_4 simulation is not used in our analysis, [6] Troposphere and stratosphere, [7] Nassar et al. [15], [8] Note that the sensitivity simulation described in Section 3.6 instead uses v5-07-08 OH fields as described in the text, [9] The stratospheric P(CO_2) is calculated online (every model timestep, 20 min) from stratospheric L(CO) (P(CO_2) = L(CO)).

In the stratosphere, Equation (6) becomes:

$$\frac{d[CO_{Strat}]}{dt} = P(CO) - L(CO) \quad (10)$$

where P(CO) represents the stratospheric production rates of CO and L(CO) represents the stratospheric CO sink based on stratospheric CO loss frequencies. Both quantities are from the NASA Global Modeling Initiative model.

The simulated CO_2 throughout the atmosphere is based on Equation (11):

$$\frac{d[CO_2]}{dt} = E_{CO_2} + P(CO_2) + D_{CO_2} \quad (11)$$

where E_{CO_2} represents the surface (fossil fuel, biomass burning, biofuel, shipping) and 3-D (aviation) emissions, P(CO_2) accounts for the 3-D chemical production from the oxidation of CO, and D_{CO_2} represents the net contribution from ocean exchange, balanced and net annual terrestrial exchange. Note that D_{CO_2} can be positive or negative since these processes have negative values in regions where they act as a net sink and positive values where

they act as a net source. Analogous to the CO simulation, the $P(CO_2)$ term is a monthly averaged archived field that was obtained with the v8-02-01 GEOS-Chem 4° × 5° full chemistry simulation from the simulated monthly CO loss rates (L(CO)) as described by Nassar et al. [15], assuming that the CO_2 production is equal to the CO loss:

$$P(CO_2) = L(CO) \quad (12)$$

Some of the emission inventories used in the CO_2 simulation already include CO_2 from CO oxidation (effectively assuming a prompt oxidation of precursors at the point of emission), but these amounts are only in the form of surface emissions rather than distributed throughout the atmosphere, leading to a bias in the model [14]. With the inclusion of a 3-D chemical source in the CO_2 simulation, this bias needs to be corrected by subtracting the CO_2 chemical production "emitted" at the surface (in the emission inventories) from the total CO_2. Nassar et al. [15] quantified a 0.825 Pg C yr^{-1} global annual value for this surface correction based on emissions of all reactants that undergo oxidation to CO_2 and are included in emission inventories. This includes emissions from fossil fuel, biospheric CH_4 (wetlands, ruminants, rice, termites, landfill) and biospheric NMVOC emissions (isoprene and monoterpene). The emission inventories used for biofuel and biomass burning explicitly account for CO_2, CO, CH_4 and NMVOC separately; hence, no surface correction is applied.

2.2. Coupled Geos-Chem Simulation

Our updates couple CH_4, CO and CO_2 based on the chemical loss and production reactions between these species, providing a single, self-consistent simulation. A schematic diagram of the coupling is shown in Figure 1.

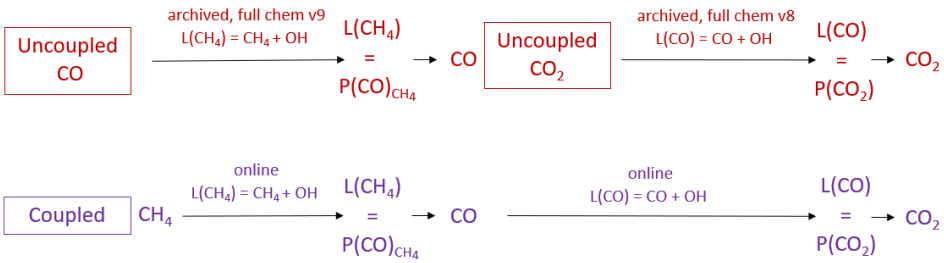

Figure 1. Schematic diagram of the tropospheric uncoupled carbon monoxide (CO) and carbon dioxide (CO_2 simulations (top) versus the coupled CH_4–CO–CO_2 simulation (CH_4 methane, bottom). The diagram also shows the model version (i.e., full chemistry simulation) used for the creation of the loss and production fields in the uncoupled simulation. Colors correspond to simulations shown in subsequent sections (see text for details). Note that both simulations use the same CO production from non-methane volatile organic compounds ($P(CO)_{NMVOC}$) field described in Sections 2.1 and 2.2 (not shown on diagram).

The starting point of the coupled simulation is the calculation of CH_4 based on Equations (4) and (5). The tropospheric CH_4 loss rates are calculated from the oxidation of tropospheric CH_4 by OH at every time step. As before, a 100% yield of CO from CH_4 oxidation is assumed [4], and the tropospheric CH_4 loss is passed to the CO part of the simulation at every timestep as the chemical production of CO from CH_4 ($P(CO)_{CH_4}$) in the troposphere. The calculation of the CO production in the stratosphere and from NMVOCs uses the same method as in the uncoupled CO-only simulation. In the troposphere, the total chemical production of CO (P(CO)) is equal to the sum of the archived $P(CO)_{NMVOC}$ field and the now-online calculated $P(CO)_{CH_4}$. The global tropospheric $P(CO)_{NMVOC}$ term is equal to 480 Tg CO yr^{-1} in both the coupled and uncoupled CO simulations for each simulation year.

The chemical production of CO_2 ($P(CO_2)$) is then calculated from the simulated CO loss from the oxidation of CO by OH in the troposphere and from the archived CO loss in

the stratosphere. As in the uncoupled version, a 100% yield of CO_2 from CO is assumed [15]. For the chemical surface correction, due to the inclusion of the chemically produced CO_2 in other emission inventories, we retained the same correction method and values as in the uncoupled simulation [15].

We used consistent archived OH fields (from v9-01-03) for all aspects of the simulation. We also note that our coupled simulation does not require running additional full chemistry simulations to create the chemical production fields, and therefore allows users to easily update the OH fields used for the oxidation of the three species (and online calculation of the chemical production terms) as new model versions become available.

The new coupling now allows for time-specific changes in and tracking of the chemical production terms. This is an improvement of the uncoupled simulations, where the prescribed fields were based on simulations of specific prior years and therefore could not capture the year-specific variations and dependencies between these gases. In the uncoupled simulations, all of the prescribed chemical production and loss fields are monthly mean values, whereas, with the coupled simulation, these fields are calculated online at every timestep (i.e., 20 min), allowing us to track the day-to-day and diurnal variability of the simulated chemical production terms.

2.3. Experimental Design

Our aim in this work was to compare the newly coupled simulation to the default (public) v12.1.1 uncoupled simulations currently used by the GEOS-Chem community. All aspects of the coupled and uncoupled simulations not associated with the chemical coupling were kept as consistent as possible with the public versions of the uncoupled simulations. The only two exceptions were: (i) the inclusion of a diurnal scaling to the OH field used for CH_4 oxidation in the troposphere and (ii) the use of the Quick Fire Emissions Dataset (QFEDv2, Darmenov and da Silva [45]) for CO_2 emissions (further details in Section S1). The former provided consistency between carbon gases in terms of the treatment of diel OH variability (which was already included for CO but not for CH_4), and the latter ensured that we could use consistent biomass burning emissions for all three species.

We ran both the uncoupled and coupled simulations from January 2005 through December 2017. The meteorological inputs for GEOS-Chem come from the Modern-Era Retrospective analysis for Research and Applications, Version 2 (MERRA2) reanalysis developed by the NASA Global Modelling and Assimilation Office (GMAO). The native horizontal resolution of MERRA2 is $0.5^\circ \times 0.625^\circ$. We ran the simulations at $2^\circ \times 2.5^\circ$ horizontal resolution with 47 vertical levels. We used 10 min as the transport and convection timestep and 20 min for the chemistry and emissions timestep. The production and loss terms used by each simulation are shown in Table 1, with additional common emission fields (i.e., source and sink processes) in Table S1. For simulation periods that are outside of the specified inventory time range, the model re-used the data from the closest year.

Based on the recommendation from the GEOS-Chem carbon cycle working group, both the uncoupled and coupled simulations were initialized with a 10-year spinup for CO_2 and CH_4 using 2005 as a base spinup year, whereas, for CO, the model was spun up for 6 months in 2005. The spinup was carried out with the uncoupled v11-01 simulations described in Bukosa et al. [10]. The initial fields prior to the spinup were based on year 2005 for CO_2 and 2010 for CH_4. Due to the increasing trend of CO_2 and CH_4 in the atmosphere, each spinup year (repeating year 2005) adds the yearly growth rate of 2005 to the modeled CO_2 and CH_4 values, leading to globally higher simulated values relative to measurements. The global modeled growth of CO_2 and CH_4 in 2005 at the surface is 1.41 ppm yr^{-1} and 0.96 ppb yr^{-1}, respectively. We quantified the overall offset by calculating the difference between the modeled CO_2 and CH_4 values at the end of the 10-year spin-up (calculated for 1 January 2005) and measurements at baseline NOAA GGGRN sites (Barrow, Mauna Loa, American Samoa (Tutuila) and South Pole, average value for January 2005). The resulting offset was 14 ppm for CO_2 and 45.8 ppb for CH_4, and we subtracted this offset from the

CO_2 and CH_4 initial fields prior to the simulations. Due to differences between emission inventories used in Bukosa et al. [10] and those used here, we used the first simulation year (2005) as an additional spinup year for all three gases.

3. Results and Discussions

3.1. Chemical Production Budgets

The main terms impacted by the coupling of CH_4, CO and CO_2 are the production of CO from CH_4 ($P(CO)_{CH_4}$) in the troposphere and the production of CO_2 from CO ($P(CO_2)$). Furthermore, the changes in these terms also impact the total source budgets for CO and CO_2 and the sink term for CO (loss of CO by OH (L(CO))). The global and hemispheric budgets for the chemical production for both coupled and uncoupled versions of the model along with known literature values are shown in Table 2. The annual global budgets of the chemical production terms $P(CO)_{CH_4}$ and $P(CO_2)$ from the uncoupled and coupled simulations are shown in Figure 2, with their regional distributions in Figures S5 and S6.

Table 2. Global and hemispheric budgets (SH—Southern Hemisphere, NH—Northern Hemisphere) for CO production from CH_4 ($P(CO)_{CH_4}$ in Tg CO yr^{-1}) and CO_2 production from CO ($P(CO_2)$ in Pg *C* yr^{-1}) from the uncoupled (U) and coupled (C) simulations, as well as literature values for the global budgets. The budgets from the simulations are shown as a multi-year mean based on years 2006–2017. The range of values for individual years is shown in the parentheses.

		Global		NH		SH	
Chemical Terms	**Prior Work**	**U**	**C**	**U**	**C**	**U**	**C**
$P(CO)_{CH_4}$	760–1086 [1,2,3,4,5,6]	902 [7] (901–905) [7]	937 (913–960)	521 [7] (520–522) [7]	536 (522–549)	381 [7] (380–382) [7]	401 (390–411)
$P(CO_2)$	1.04–1.1 [8,9]	1.1 [10] (1.08–1.11) [10]	1.03 (1.01–1.05)	0.67 [10] (0.63–0.68) [10]	0.62 (0.62–0.63)	0.43 [10] (0.43–0.46) [10]	0.40 (0.39–0.42)

[1] Holloway et al. [27], base year: not defined; [2] Bergamaschi et al. [25], base year: 1993–1995; [3] Duncan et al. [4], base year: 1988–1997; [4] Arellano Jr. and Hess [28], base year: 2000–2001; [5] Stein et al. [29], base year: 2008; [6] Zeng et al. [30], base year: 2004; range based on different model simulations. [7] Fisher et al. [17], base year: 2009–2011 average; [8] Nassar et al. [15], base year: 2000–2009; [9] Suntharalingam et al. [14], base year: 1988–1997; [10] Nassar et al. [15], base year: 2006–2010.

The results from our coupled simulation remain consistent with the range of values found in prior work. The coupled simulation shows stronger $P(CO)_{CH_4}$ than the fields used by the uncoupled simulation. The stronger chemical production is mainly driven by different CH_4 levels between the coupled simulation and the full chemistry simulation (used as the input in the uncoupled CO simulation). The $P(CO)_{CH_4}$ calculation in both simulations is based on the same OH version (v9-01-03), although minor differences exist due to the temporal resolution of the OH fields (monthly OH fields with diurnal scaling for coupled, hourly for uncoupled). The coupled $P(CO)_{CH_4}$ values are stronger than the uncoupled values for all years and for both hemispheres (11–55 Tg CO yr^{-1} difference). This difference represents 0.5–2.3% of the total CO source in the coupled simulation. The CO_2 chemical source shows weaker values in the coupled simulation relative to the uncoupled one (0.04–0.09 Pg *C* yr^{-1} difference). This difference represents 0.3–0.7% of the total CO_2 source in the coupled simulation. The stronger uncoupled $P(CO_2)$ values are a result of different CO amounts used for the CO loss calculation between the coupled and full chemistry (used as the input for the uncoupled) simulations, as well as more abundant OH used to calculate L(CO) for the uncoupled simulation (v8-02-01, Figure S2) relative to the OH field used in the coupled simulation (v9-01-03).

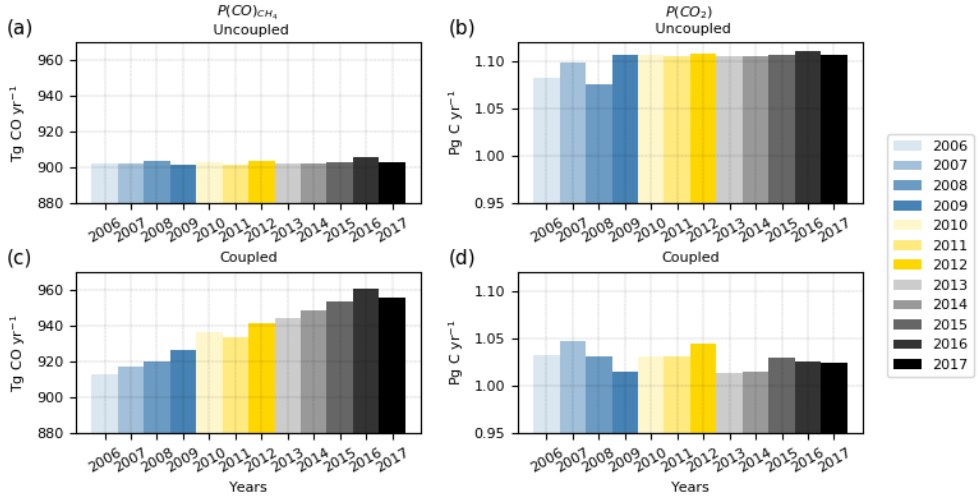

Figure 2. Annual values of the global chemical production term budgets for CO production from CH_4 (**a**,**c**) and CO_2 production from CO (**b**,**d**) from the uncoupled (**a**,**b**) and coupled (**c**,**d**) simulations. Regional distributions are shown in Figures S5 and S6.

Figure 2a,b show that there is some very minor inter-annual variability in the chemical production fields simulated by the uncoupled simulation despite the fact that the input chemical production fields used in this simulation do not vary inter-annually for CO (based on 2009–2011 average values) and do not vary inter-annually after year 2010 for CO_2. This small variability in the uncoupled simulation is exclusively driven by: (1) leap years in 2008, 2012 and 2016 that lead to a larger total annual production and (2) interannual variability in the meteorological fields (e.g., pressure levels, tropopause height) affecting the calculation of the total tropospheric budget.

The inter-annual variability of the chemical fields is one of the key benefits of the coupled simulation. We found a consistent increasing trend in $P(CO)_{CH_4}$ over the 2006–2017 period in the coupled simulation (Figure 2c) due to increasing atmospheric CH_4 concentrations leading to an increased CH_4 loss and associated CO production. The $P(CO)_{CH_4}$ increase is the most pronounced in tropical regions (Figure S5). For P(CO_2), we do not observe a trend in the coupled results. The 2006–2010 P(CO_2) results do not entirely match the inter-annual variability shown in the uncoupled fields. The year-to-year change of the chemical fields in the coupled simulation is driven by the inter-annual variability of the emission fields used to simulate CH_4 and CO (Tables 1 and S1). Some of the emission-driven variability may potentially be linked to El Niño Southern Oscillation (ENSO). For example, we observe the strongest growth in $P(CO)_{CH_4}$ during 2009/2010 and 2015/2016, which coincide with moderate and strong El Niño years, while we find no growth during 2010/2011, a strong La Niña year, highlighting the potential impact of climate anomalies on the chemical terms. However, we note that 2016 is also a leap year, which will also impact the production increase. Different ENSO-triggered CH_4 processes lead to opposite changes in CH_4: during El Niño events, wetland emissions are reduced, whereas biomass burning emissions are enhanced [46–49]. Our coupled simulation shows that these changes can have an imprint on the chemical production of CO that is not captured in the uncoupled simulation. The availability of OH via CO also impacts the CH_4 interannual variability; however, we were unable to quantify the OH-driven changes here as none of our simulations included OH inter-annual variability or OH-feedbacks. We recommend that future updates to the coupled simulation prioritize the inclusion of a CO–OH–CH_4 feedback in the calculation [34,50].

Figure 3 shows the budgets throughout the year for each chemical term in different latitudinal bands. Figure 3a shows that both the uncoupled (red) and coupled (indigo) $P(CO)_{CH_4}$ have a similar annual cycle, with an overall stronger production in the coupled simulation. The coupled simulation also shows more variability due to the year-specific

CH_4 loss, with the most variability in tropical regions. Although covering a shorter time period with year-specific fields, from 2006 to 2010, the uncoupled P(CO_2) values show more variability than in the coupled version (Figure 3b). The uncoupled simulation also shows stronger P(CO_2) values in all latitudinal bands. The largest difference between simulations is during December–March, mostly in Northern Hemisphere (NH) tropical and Southern Hemisphere (SH) mid-latitude regions.

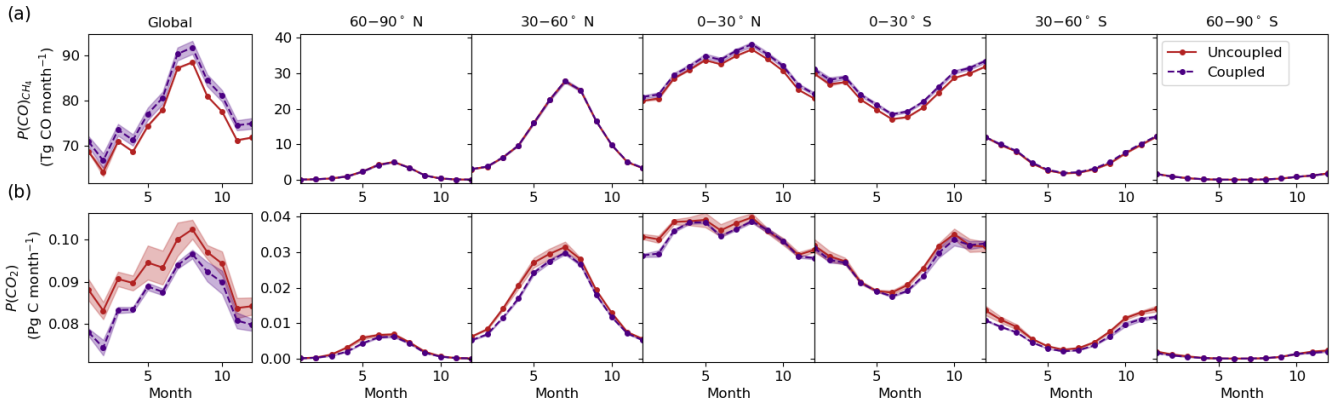

Figure 3. Monthly total atmospheric column CO production from CH_4 (**a**) and CO_2 production from CO (**b**), with 1 standard deviation (shaded region), from the uncoupled (red) and coupled (indigo) simulation averaged for 2006–2017 and summed globally (left) and over different regions (right).

3.2. Chemical Source Contributions

Due to the linearity of the GEOS-Chem carbon greenhouse gas simulations, in addition to simulating the total amount of each gas, we can also quantify the mole fractions of individual processes (referred to as tracers). These include the CO_2 mole fraction from CO_2 chemical production (CO_{2CO}) and the CO mole fraction from CO production from CH_4 (CO_{CH_4}). Figure 4 shows these chemical production tracers (Figure 4a,b), as well as the total CO and CO_2 mole fractions (Figure 4c,d) at the surface for different latitudinal bands. Note that, in contrast to the CO source tracers, where the atmospheric sink terms (e.g., OH) are applied to each tracer, for CO_2, there is no sink applied to the different source tracers. This leads to a trend in CO_{2CO} and its accumulation in the atmosphere. To highlight differences in the seasonal cycle, we detrended the CO_{2CO} data shown in Figure 4b,d and added the mean 2006–2017 yearly growth rates.

Implementing the online calculation of the chemical terms results in higher CO_{CH_4} values in the coupled simulation relative to the uncoupled simulation, along with a stronger variability (Figure 4a), similar to the production rates (Table 2, Figure 3a). An average 0.8 ± 0.5 ppb difference is present across the NH between the coupled and uncoupled results, whereas, in the SH, we find a larger difference of 1.4 ± 0.5 ppb. Both the coupled and uncoupled simulations show similar seasonal cycles. The difference in CO_{CH_4} is also reflected in the total amounts of CO (Figure 4c), leading to slightly higher global surface CO values in the coupled simulation. $P(CO)_{CH_4}$ and CO_{CH_4} show a seasonal cycle, with the maximum production during NH summer and minimum during winter, which is the opposite of the seasonal cycle of the total CO mole fractions.

The CO_{2CO} mole fractions also show a similar seasonal cycle between the two simulations in both hemispheres (Figure 4b). The uncoupled simulation shows a stronger yearly global surface growth rate of 0.52 ppm yr^{-1} due to the stronger chemical production, whereas the coupled simulation shows a weaker growth rate of 0.48 ppm yr^{-1} due to weaker production. Overall, the coupling does not significantly impact the resulting CO_2 mole fractions between simulations. The differences between the coupled and uncoupled simulations are too small to be reflected in the total CO_2 surface values (Figure 4d). As already highlighted, P(CO_2) is a 3-D source; hence, the signal of this source in the surface mole fractions is small relative to the other more dominant CO_2 surface fluxes.

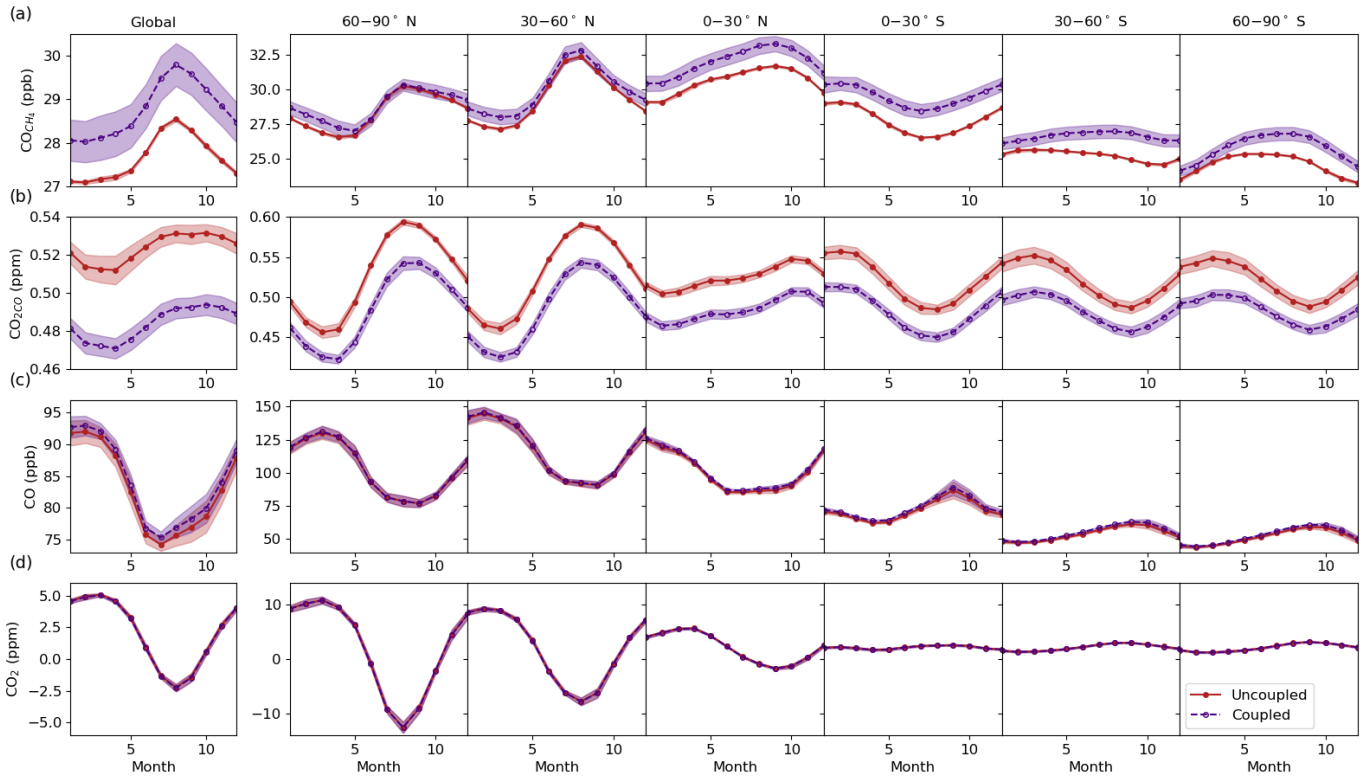

Figure 4. Surface mole fractions from chemical production of CO_{CH_4} (**a**) and CO_{2CO} (**b**) and total CO (**c**) and CO_2 (**d**) mole fractions from the uncoupled (red) and coupled (indigo) simulations with 1 standard deviation (based on 2006–2017 average values). Note that the CO_2 values are detrended and added to the mean 2006–2017 yearly growth rates.

3.3. Global Distribution

Figure 5 shows the total column chemical production of CO from CH_4 with corresponding CO_{CH_4} mole fractions at the surface and a 500 hPa altitude from the coupled simulation, as well as the difference between the coupled and uncoupled simulations. Figure 6 is the same as Figure 5 but for the chemical production of CO_2 and the CO_{2CO} mole fractions. For CO_2, we additionally removed the long-term trend from the CO_{2CO} mole fractions. The seasonal changes of both the production terms and mole fractions are shown in Figures S7–S10 for CO and Figures S11–S14 for CO_2.

The online calculation of $P(CO)_{CH_4}$ has a small impact on its global spatial distribution; both the coupled and uncoupled simulations show similar distributions (Figure 5a,d). The simulations used the same OH fields; hence, the differences in $P(CO)_{CH_4}$ are driven by the different handling of the CH_4 values before the OH loss is applied. The main difference between the two simulations is the stronger $P(CO)_{CH_4}$ over tropical ocean regions and weaker $P(CO)_{CH_4}$ over NH land regions in the coupled version. On a yearly scale, the surface CO_{CH_4} mole fractions from the coupled simulation show higher values above both ocean and land regions (Figure 5e), as a result of the stronger $P(CO)_{CH_4}$ over tropical ocean regions. A similar behavior is observed at 500 hPa; however, the differences are smaller and more diffuse. We find the same differences throughout the seasons (Figures S7–S10). We further discuss the simulated mole fractions and the impact of the coupling on total *CO* in Section 3.5.

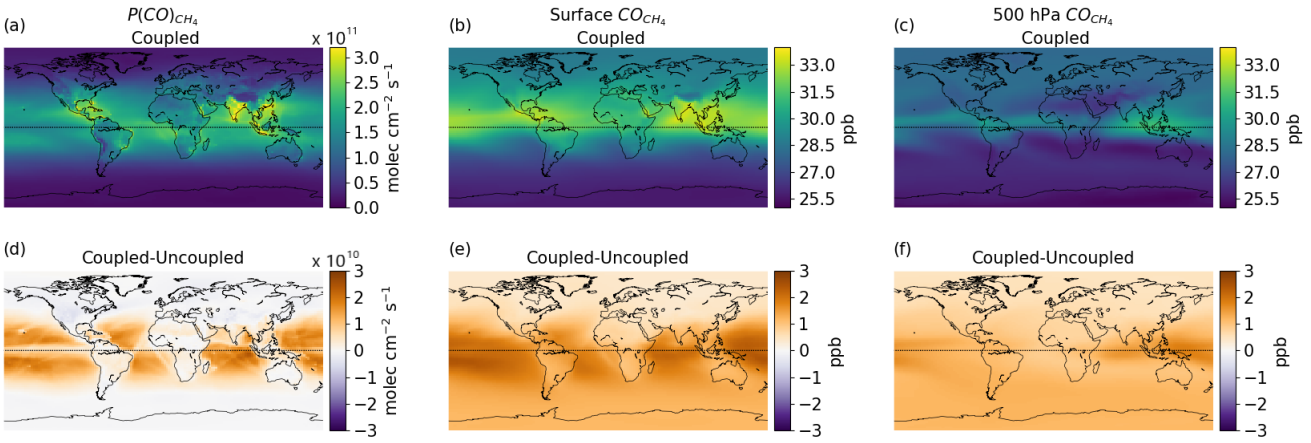

Figure 5. Average 2006–2017 total column CO chemical production from CH_4 (**a**) and corresponding mole fractions (i.e., CO_{CH_4}) at the surface (**b**) and at 500 hPa (**c**) from the coupled simulation, along with the difference in each field between the coupled and uncoupled simulation (**d**–**f**).

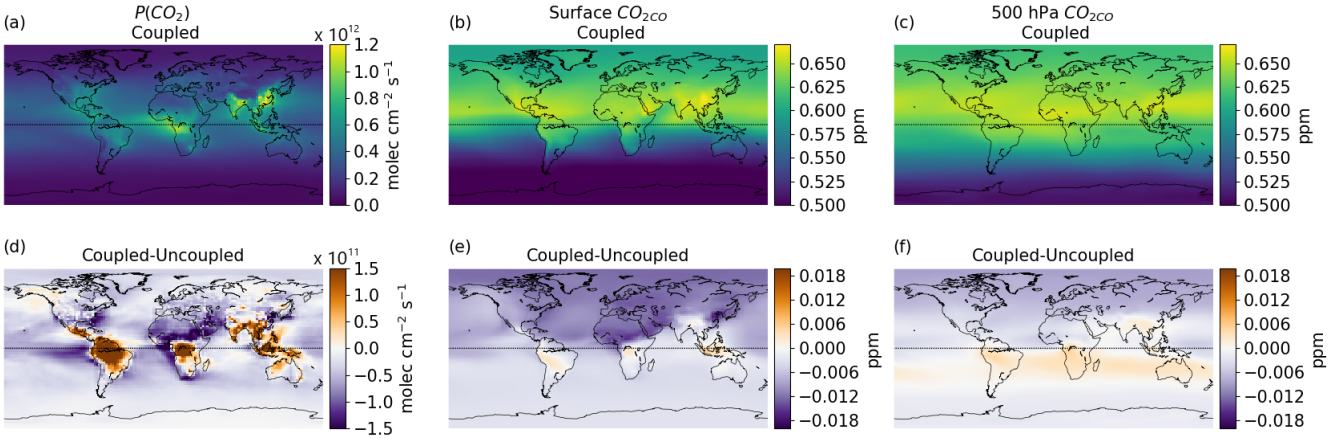

Figure 6. Average 2006–2017 total column CO_2 chemical production from CO (**a**) and corresponding mole fractions (i.e., CO_{2CO}) at the surface (**b**) and at 500 hPa (**c**) from the coupled simulation, along with the difference in each field between the coupled and uncoupled simulation (**d**–**f**).

The coupled simulation shows stronger $P(CO_2)$ (Figure 6d) in certain land regions (South America, Central Africa, Indonesia, parts of East Asia and Australia) despite the annual global chemical source being weaker than in the uncoupled simulation. Moreover, in the uncoupled simulation, there is almost no $P(CO_2)$ observed above the Amazon [15]; however, our results suggest substantial $P(CO_2)$ in this region. The difference patterns appear to be mostly independent of season (Figures S11–S14). The chemical production is overall weaker above the ocean in the coupled simulation for all seasons; however, the coupled simulation does show stronger $P(CO_2)$ during certain periods in tropical and NH mid-latitude regions. The stronger $P(CO_2)$ in the coupled simulation above South America, Central Africa, Indonesia, parts of East Asia and Australia is present in all seasons, but with the strongest contribution during September–November. South America, Central Africa and northern Australia are characterized by strong biomass burning, especially during the SH dry season, when frequent fires are observed (September–November), emitting large amounts of CO into the atmosphere [51]. Our coupled model simulates the $P(CO_2)$ in these regions during the fire season to be stronger than the previous fields used in the uncoupled simulation. The stronger $P(CO_2)$ from the coupled simulation in other regions such as East Asia and North America points to enhanced anthropogenic CO emissions that lead to a stronger chemical production of CO_2. In addition to the primary CO emissions, the secondary production of CO from NMVOC could also have a significant

impact on the P(CO_2) in regions where we observe differences. Different model versions were used to save the P(CO)$_{NMVOC}$ and P(CO_2) in the uncoupled simulations, as discussed in Section 2. The updated chemistry between model versions would additionally impact the P(CO_2) through the CO production from NMVOC in regions where we expect a significant contribution from this production term (e.g., the Amazon). The spatial distribution of the surface mole fractions is similar between simulations, with lower values overall in the coupled simulation, especially in the NH, due to the globally stronger P(CO_2). However, the coupled simulation does show more abundant CO_{2CO} over tropical land regions, with stronger P(CO_2), and over the SH during June-November (Figures S13 and S14). The higher coupled simulation CO_{2CO} values over tropical land regions are more pronounced at 500 hPa.

3.4. Vertical Latitudinal Distribution

Figure 7 shows the vertical latitudinal distribution of $P(CO)_{CH_4}$ and P(CO_2) for different months, averaged for 2006–2017, as well as the difference between the uncoupled and coupled simulations. The strongest $P(CO)_{CH_4}$ in the coupled simulation occurs between the surface and 3 km altitude. For most months, this chemical production is stronger in the NH than in the SH; however, around November we observe stronger production in the SH, potentially due to biomass burning and wetland activity, that leads to enhanced CH_4 levels and its subsequent loss driving CO production. Although the strongest production occurs between 50° S–50° N, we also observe production in Antarctic regions in December–January and in Arctic regions in May–July, corresponding to their summer periods. Production is stronger in the Arctic than in the Antarctic due to higher CH_4 levels and the stronger loss in the NH. As for the global spatial distribution results, the coupling has a small impact on the vertical distribution (Figure 7c, stronger production in the coupled than in the uncoupled).

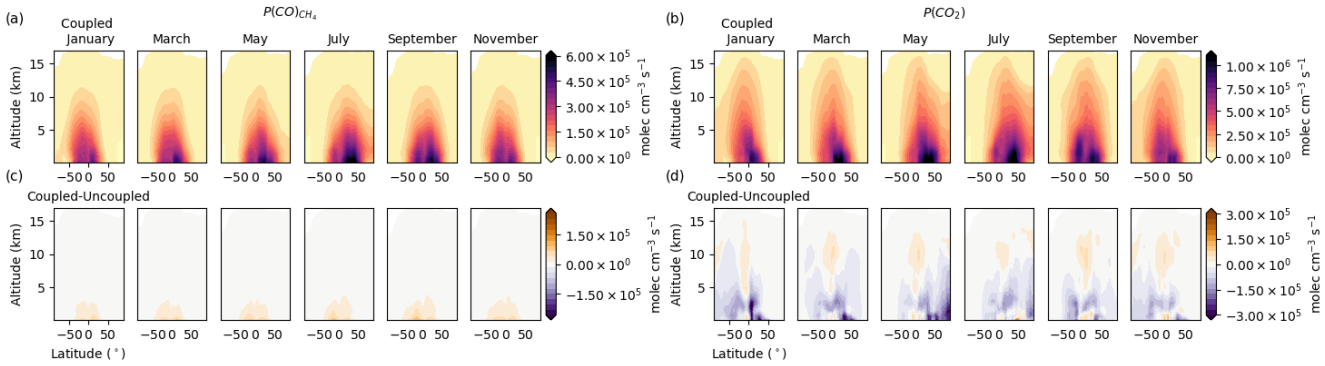

Figure 7. Vertical latitudinal distribution of the coupled CO chemical production from CH_4 (**a**) and CO_2 chemical production from CO (**b**) and the coupled–uncoupled differences (**c**,**d**) over different months, averaged over 2006–2017.

The strongest CO_2 chemical production in the coupled simulation occurs between the surface and 4 km altitude, and CO_2 is produced chemically up to 15 km (Figure 7b). From January–July, we observe stronger production in the NH, with the strongest production in tropical regions at the beginning of the year, moving toward higher latitudes by July. Based on the distribution of this source in the NH (Figure 6), strong production occurs over China and India from anthropogenic CO, with mixed biomass burning influence from other regions. For the remaining months, both hemispheres show strong P(CO_2), with the SH showing stronger production in September, presumably due to additional biomass burning in the tropics (e.g., Indonesia, Australia, Africa, S America). Using an uncoupled version of the CO_2 simulation, Nassar et al. [15] did not find a biomass burning contribution over the Amazon; however, our coupled simulation, as already discussed, suggests a significant contribution from this region. Relative to the uncoupled simulation, the coupled simulation shows weaker production in mid-latitude and polar regions, with a stronger contribution

in the tropics at surface levels and above 5 km. The Arctic and Antarctic regions show weaker production in the coupled simulation.

3.5. Model Evaluation with Column, Surface and Aircraft Measurements

We validated the new coupled simulation against global column retrievals and calibrated surface flask and aircraft in situ measurements (Figure 8, Table A1 in Appendix A). Long-term time series of column-averaged dry-air mole fractions of CO and CO_2 were measured by TCCON [52]. In addition, long-term time series of surface mole fractions exist at different sites across the globe as part of NOAA GGGRN (Dlugokencky et al. [53,54]). For a vertical profile comparison, we used aircraft measurements from the ATom campaigns [55]; for both CO_2 and CO, we used the merged ATom data product collected from the NOAA-Picarro and Harvard Quantum Cascade Laser System instrument.

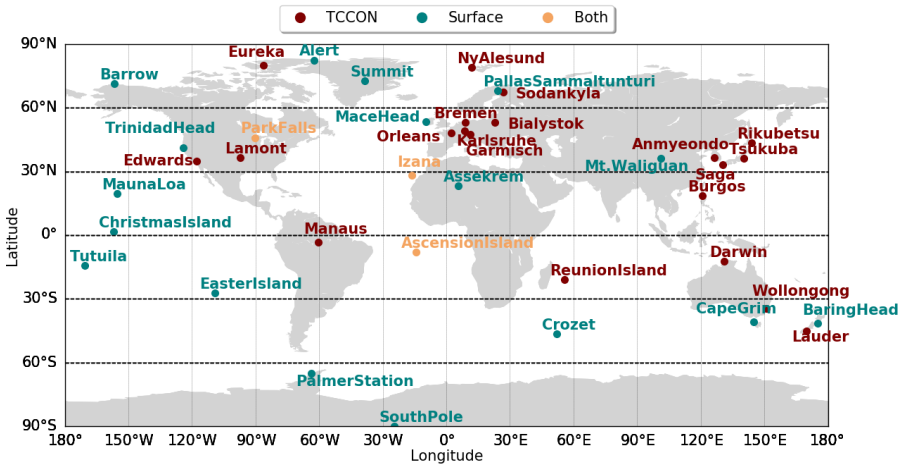

Figure 8. Locations of the flask surface sites from the NOAA Global Greenhouse Gas Reference Network (NOAA GGGRN, turquoise, Dlugokencky et al. [53,54]) along with sites that measure column-averaged dry-air mole fractions as part of the Total Carbon Column Observing Network: (TCCON, red, https://tccondata.org/, accessed on 10 march 2023) and sites that are both part of TCCON and NOAA GGGRN (orange). For site details, see Table A1 in Appendix A.

We used column measurements from TCCON as the main data product to highlight the differences between the coupled and uncoupled simulations. Both the CO and CO_2 chemical sources are produced throughout the column; hence, relative to surface measurements, these measurements are more representative of the impact of chemical production on the total amounts of the gases. In order to compare the total CO and CO_2 model output with the column-averaged measurements, we converted the modeled mole fractions to column-averaged dry-air mole fractions (X_{gas}) by dividing the vertical column of the gas of interest (Ω_{gas}) with the total dry-air column (Ω_{O_2}) based on the method described by Wunch et al. [56]:

$$X_{gas} = 0.2095 \frac{\Omega_{gas}}{\Omega_{O_2}} \tag{13}$$

and smoothed according to Equation (14) [57]:

$$c_s = c_a + h^T a^T (x_m - x_a) \tag{14}$$

where c_s represents the smoothed column model dry-air mole fraction, c_a is the TCCON a priori column dry-air mole fraction, h^T represents the vertical column summation, a^T is the TCCON averaging kernel and x_m and x_a are the model and a priori dry-air mole fraction profiles.

The modeled vertical profiles were saved at a daily temporal resolution and extracted for the closest grid box to each TCCON station. For the comparison with surface measure-

ments, we extracted the grid points at the lowest level in the model. For the comparison with aircraft measurements, model outputs were saved for grid boxes corresponding to the measured time, latitude, longitude and level along the plane flight track. Both the aircraft measurements and modeled output were averaged to the model temporal (20 min) and spatial ($2^\circ \times 2.5^\circ$) resolution to calculate one average value for each unique grid-box–time-step combination.

Both the column and surface measurements are impacted by data gaps. In order to minimize the impact of the non-continuous measurements and inconsistent measurement time periods on the analysis, we used a consistent time period (2010–2017) when analyzing the measurement–model differences. We found the fewest data gaps during this time period; however, a few sites are still subject to missing measurements (column: Ny Alesund, Rikubetsu, Edwards, Anmyeondo, Saga, Ascension Island, Reunion; surface: Trinidad, Easter Island, Christmas Island). Due to short timeseries at the Manaus and Burgos TCCON sites, we excluded them from the plots representing the measurement–model differences in the next section (Section 3.5.1); however, the full timeseries at all sites can be found in Figures S15–S18.

3.5.1. Comparison with Column Measurements

Figure 9 shows the differences between the modeled values (uncoupled and coupled) and measurements at different TCCON sites for CO (Figure 9a–e) and CO_2 (Figure 9f–j) plotted against the latitude of each site. We also show the normalized mean bias between the modeled and measured values on each plot. Mid-latitude European sites (Białystok, Bremen, Karlsruhe, Orléans and Garmisch, grouped into Other EU sites) show similar results; hence, we only present their mean value. The timeseries comparison of the total CO, CO_{CH_4}, CO_2 and CO_{2CO} mole fractions for each site can be found in Figures S15 and S16.

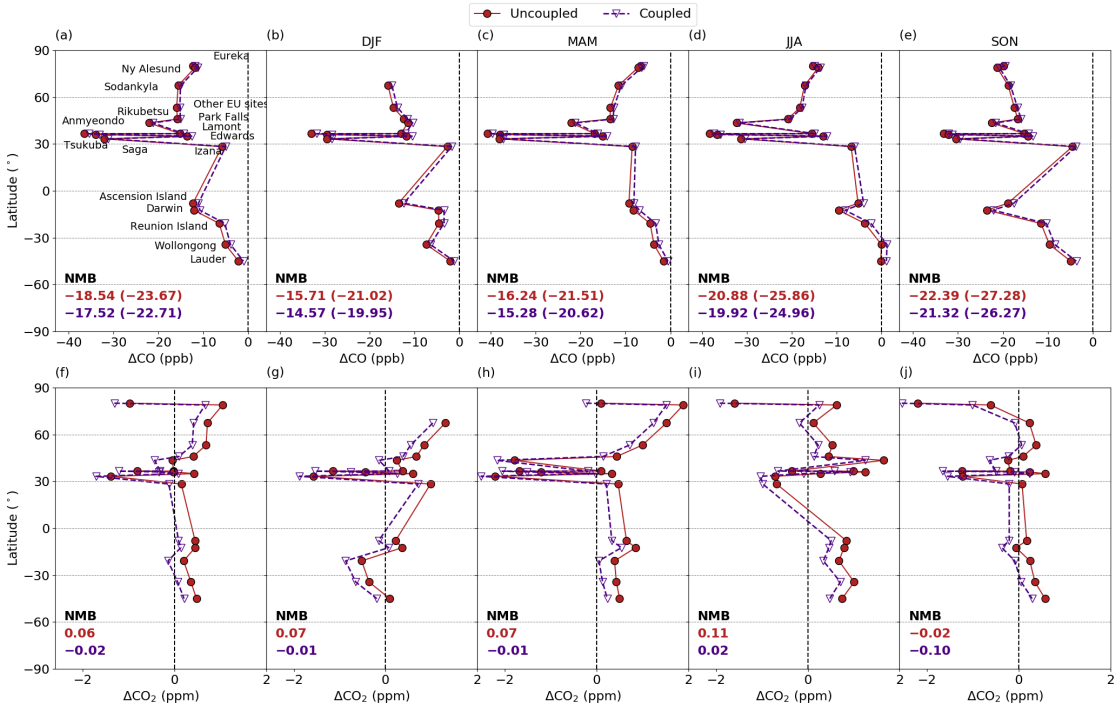

Figure 9. Column-averaged mole fraction model–measurement differences (uncoupled (red) and coupled (indigo)) for CO (**a**–**e**) and CO_2 (**f**–**j**) as a function of latitude, averaged for 2010–2017, with annual values (**a**,**f**) and for different seasons: December–January–February (DJF,: (**b**,**g**)) , March–April–May (MAM, (**c**,**h**)), June–July–August (JJA, (**d**,**i**)), September–October–November (SON, (**e**,**j**)). The numbers inset represent the normalized mean bias (NMB). For CO, we also show the NMB based on the unscaled CO values (shown in the parentheses).

The coupled CO results lead to a smaller bias between the modeled and measured values in both hemispheres and all seasons (except at SH mid-latitude sites, Lauder and Wollongong in June–July–August). Differences in the CO values are driven by differences in the CH_4 loss calculation, and we find that the stronger CH_4 loss in the coupled simulation leads to a smaller model–measurement bias, suggesting that this term was potentially underestimated in the uncoupled simulation. The distribution of the model–measurement differences between sites is consistent between the coupled and uncoupled simulation but with larger differences for sites in the SH. Previous studies showed that CO values in the SH are dominated by CH_4 and NMVOC oxidation [17,30,58]; hence, the larger SH offset between the coupled and uncoupled simulation is driven by the dominance of chemical production relative to other CO sources.

On a yearly scale and for all seasons, the smallest CO model–measurement bias is present at sites closest to the South Pole, with an increasing negative bias (i.e., underestimation of the modeled values compared to measurements) toward the NH. In the NH, the biases show a smaller latitudinal dependence than in the SH, presumably due to the larger differences in the CO sources between regions/sites. Differences in the modeled–measured values throughout the seasons highlight potential contributors to the observed biases. In the SH, we find a stronger negative bias during austral spring (September–October–November), while the seasonal dependence in the NH is more variable. The larger SH bias during austral spring suggests an underestimated biomass burning source, since this period aligns with the burning season in the SH. Due to uncertainty in the TCCON bias-correction to in situ scales for CO, we also compared our modeled CO with the unscaled TCCON CO values that are higher by approximately 7%. For all sites, we obtained the unscaled values by multiplying the column CO by 1.0672. The potential TCCON bias is apparent in comparison to MOPITT (Measurements of Pollution in the Troposphere) [59] and to NDACC (Network for Detection of Atmospheric Composition Change) [60]. The resultant Normalized Mean Bias (NMB) relative to the unscaled values is also shown in Figure 9a–e. A comparison with the unscaled values further increases the negative model–measurement bias.

Relative to CO, where we observe a consistent negative bias, the CO_2 biases are more variable between both sites and seasons. On a yearly scale and for most sites, the coupled CO_2 results show a smaller model–measurement bias than the uncoupled results. The main difference between the uncoupled and coupled CO_2 values is the weaker CO_2 chemical production in the coupled simulation, suggesting that this source term might have been overestimated in the uncoupled simulation (although there could be other compensating biases). For most sites and seasons, the simulated CO_2 values are higher than the measurements (Figure 9f–j). An exception in the NH is Eureka, where there is a consistent negative bias, and NH mid-latitude sites that show either a negative and positive bias depending on the season. We find the largest model–measurement bias for the NH mid-latitude sites (30–45° N). This bias is potentially driven by a combination of biases in the terrestrial and anthropogenic emissions that dominate CO_2 variability in these regions. The sites in the 30–45° N band also show the largest biases in the CO comparisons; hence, common CO and CO_2 anthropogenic emissions might be the dominant driver of this bias. Whether or not this bias extends to NH tropical regions cannot be determined due to a lack of TCCON sites in tropical regions. Relative to the NH, the SH biases are smaller and less variable, presumably due to less variable CO_2 sources/sinks.

Overall, our coupled simulation led to a smaller model–measurement bias than the original uncoupled simulations. However, we note that the reduced bias could potentially be compensating for biases in other emissions fields and that some of the differences in the biases are small when compared to other uncertainties in the system. Further bias reductions would come from reducing uncertainties in other fluxes and transport. The inclusion of an OH feedback between species would additionally impact the model–measurement bias, especially during enhanced localized emission events (i.e., fires). As an example, strong CO emissions would lead to depleted OH values, resulting in a weaker

oxidation of CH_4 and the production of $P(CO)_{CH_4}$. This feedback is not captured in either of the simulations since the OH fields are fixed.

3.5.2. Comparison with Surface Measurements

We complemented the column measurements with surface measurements. Figure 10 shows the differences between the uncoupled and coupled simulations versus the measurements at surface sites for CO (Figure 10a–e) and CO_2 (Figure 10f–j) plotted against the latitude of each site. The timeseries comparison for each site can be found in Figures S17 and S18. Note that, relative to the column results, the surface comparison is more strongly impacted by the coarse model resolution ($2^\circ \times 2.5^\circ$). The measured and modeled column values are more representative of regional and larger-scale processes so the impact of the model resolution is weaker.

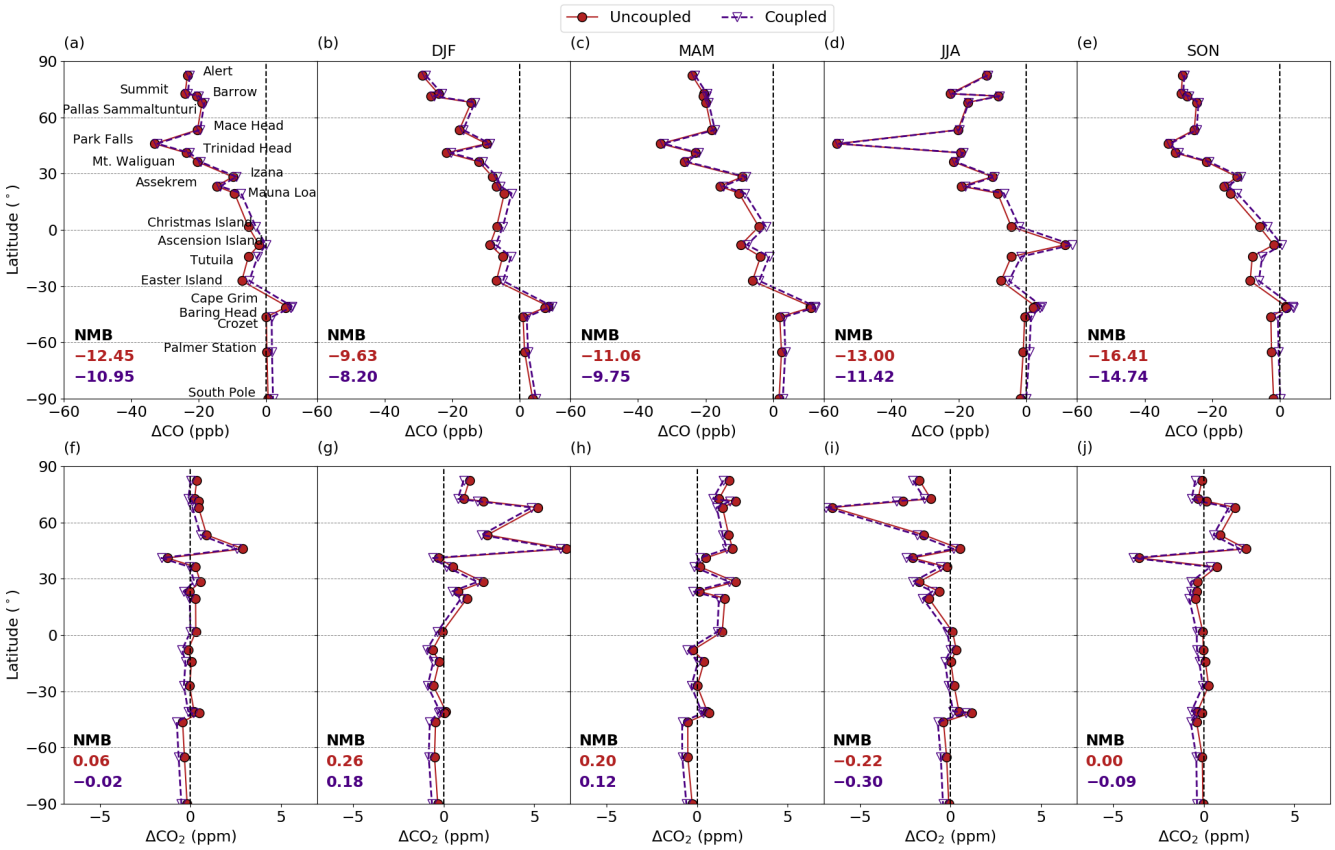

Figure 10. Surface mole fraction model–measurement differences (uncoupled (red) and coupled (indigo)) CO (**a**–**e**) and CO_2 (**f**–**j**) as a function of latitude, averaged for 2010–2017, with annual values (**a**,**f**) and for different seasons: December–January–Febuary (DJF, (**b**,**g**)) , March–April–May (MAM, (**c**,**h**)), June–July–August (JJA, (**d**,**i**)), September–October–November (SON, (**e**,**j**)).

For CO, the model–measurement biases in the surface data are similar to the column results. However, in the column data, we lacked measurements in NH tropical regions and 45–90° S, limiting us from identifying the biases. With available measurements in each latitudinal band, the surface comparison further amplifies the latitudinal dependence of the bias, increasing from the SH polar regions toward the North Pole. Relative to the column comparison, at the surface, the large bias at NH mid-latitude sites is less pronounced. The column CO values were consistently lower than the measurements; however, at the surface, we see an overestimation of the CO values for some SH sites (although a number of these sites are in regions where we lack column measurements). The overestimated values in the SH might be partially due to transport errors [61], such as the weaker vertical mixing [62,63] in the model leading to the buildup of CO in the planetary boundary layer.

Having column measurements in these regions would be beneficial when identifying the processes responsible for the observed model–measurement biases.

Differences between the surface and column comparison are more pronounced in the CO_2 data. We still find, on average, a smaller model–measurement bias in the coupled results; however, the latitudinal distribution of the biases is different relative to the column results. In the SH, we observe a consistent negative bias in the coupled results, whereas the column data pointed to a positive bias (i.e., overestimated modeled values compared to measurements). The negative bias tends to be larger for sites between 45–90° S, a region where we lack column measurements. The differences in the polar regions are potentially impacted by additional CO_2 exchange from air–sea ice interaction [64], a process that is not included in the simulation, and are still subject to large uncertainties [65]. The surface measurements in the NH tropics (where column measurements are lacking) show a positive bias during boreal winter/spring and negative bias during boreal summer/autumn.

3.5.3. Comparison with Aircraft Measurements

We further compared the simulations with aircraft measurements collected as part of ATom (campaign 1: July–August 2016, 2: January–February 2017, 3: September–October 2017 and 4: April–May 2018). Figure 11 shows the differences between the modeled and measured CO and CO_2 values during the four campaigns as a function of latitude and pressure. The spatial distributions of the differences between the modeled and measured values and CO_{CH_4} and CO_{2CO} cross-sections (Section S3) are shown in Figures S19 and S20.

The latitudinal change of the aircraft model–measurement differences for CO follows the pattern seen in both the column and surface data (a smaller model–measurement bias in the coupled simulation and, on average, underestimated modeled values compared to measurements). The negative CO bias is present during all seasons and latitudinal bands except during ATom 2 (austral summer) and ATom 4 (austral fall) south of 50–60° S. This negative bias is also present in the surface data, whereas, in the column data, we do not have sites south of 45° S. The model also underestimated the CO values compared to measurements at all vertical levels during all four campaigns/seasons (Figure 11c,g,k,o). Differences between the two simulations decrease with increasing altitudes in the model. Differences between the two simulations also decrease at higher latitudes during all ATom campaigns except ATom 2, where the difference between simulations is lowest in the SH mid-latitudes.

For CO_2, we find a consistent negative bias in all latitudinal bands except 65–70° N during ATom 2 (boreal winter). This is different from both the surface and column comparison, where we had a mixture of both negative and positive biases. Different biases in the surface, column and aircraft comparisons suggest that potential biases in vertical transport should also be explored. The coupled simulation shows a smaller model–measurement bias for both the surface and column comparison; however, for the aircraft comparison, we find a smaller bias in the uncoupled results. The model underestimated the CO_2 values compared to measurements in the uncoupled simulation, and the weaker chemical production in the coupled simulation further increased this bias. For CO_2 (in contrast to CO), the offset between the coupled and uncoupled simulations is consistent across all latitudinal bands and vertical levels.

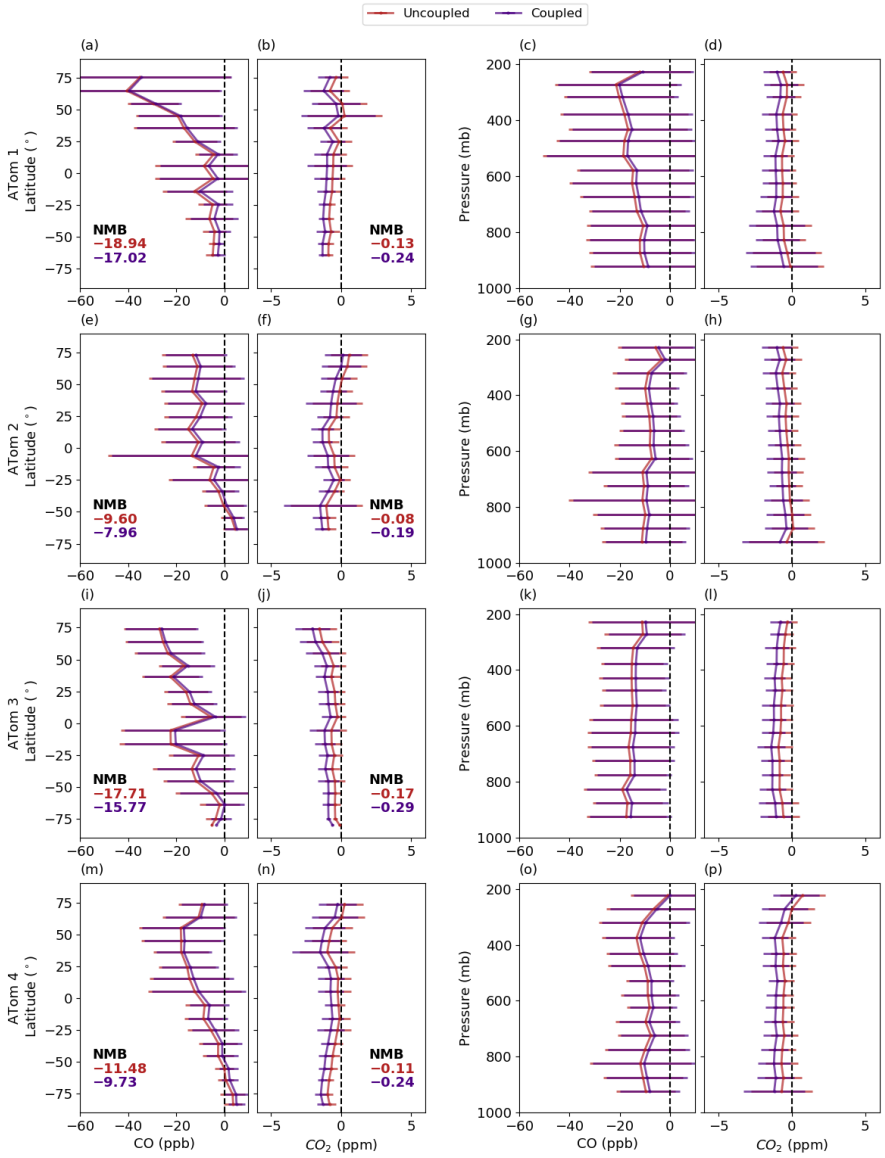

Figure 11. Aircraft model–measurement (uncoupled (red) and coupled (indigo)) CO and CO_2 differences, shown as their latitudinal (CO: (**a**,**e**,**i**,**m**) CO_2: (**b**,**f**,**j**,**n**)) and altitudinal distribution (CO: (**c**,**g**,**k**,**o**), CO_2: (**d**,**h**,**l**,**p**)) during the four Atmospheric Tomography Mission (ATom) campaigns in June–July 2016 (**a**–**d**), December–January 2017 (**e**–**h**), August–September 2017 (**i**–**l**) and March–April 2018 (**m**–**p**). Horizontal lines show standard deviation within each bin. The data are averaged into 10° latitudinal and 50 mb pressure bins.

3.6. The Importance of Consistent OH Fields

In this section, we explore the impact of inconsistent OH fields on the chemical production terms. In our coupled simulation, we used consistent OH fields (from v9-01-03) for all aspects of the simulation. However, as discussed in Section 2.1, the uncoupled simulations also rely on production and loss fields derived from the full chemistry simulation that was available at the time each capability was developed or updated, leading to differences in the resulting chemical fields. For the uncoupled simulations in the default v12.1.1 GEOS-Chem model, these fields were derived from GEOS-Chem v5-07-08 for the CH_4 simulation [44], v9-01-03 for the CO simulation [17] and v8-02-01 for the CO_2 simulation [15]. The global annual mean OH is largest in the v8-02-01 full chemistry simulation (11.8×10^5 molecules cm^{-3}) followed by v9-01-03 (11.4×10^5 molecules cm^{-3}) and v5-07-08 (10.8×10^5 molecules cm^{-3})

(http://wiki.seas.harvard.edu/geos-chem/index.php/Mean_OH_concentration, accessed on 10 March 2023). The yearly change and annual/seasonal global spatial patterns of the OH fields are shown in Figures S2–S4.

The OH disconnect inherent in the existing uncoupled simulations can introduce biases and inconsistencies in the simulated CH_4, CO and CO_2. Of most importance are inconsistencies in the archived OH fields used to calculate chemical loss rates for CH_4 and CO. Note that the uncoupled CO_2 simulation does not directly use OH (i.e., there is no CO_2 OH sink), so, for the CO_2 simulation, there is only a small and indirect influence from OH through OH-driven CO loss in the full chemistry simulation used to calculate the CO_2 chemical production fields. Here, we used the coupled model to perform an additional sensitivity simulation, retaining the default version of the OH used in the v12.1.1 uncoupled CH_4 simulation (i.e., v5-07-08 OH for the calculation of L(CH_4)) to highlight the impact of inconsistent OH fields currently in use in GEOS-Chem. We will refer to this sensitivity simulation as the *coupled-origOH* simulation.

We performed a 1 year simulation (2006) to analyze the impact of the OH disconnect. Both the coupled and *coupled-origOH* simulations were initialized with the same CH_4, CO and CO_2 initial conditions and both simulations used the same OH fields (v9-01-03) to calculate L(CO) and P(CO_2). The differences in the modeled values between the two simulations are exclusively driven by differences between the v5-07-08 and v9-01-03 OH fields used to calculate L(CH_4) and, by extension, $P(CO)_{CH_4}$. Differences between the OH fields are shown in Figures S2–S4. Briefly, the v9-01-03 OH shows higher values, with a peak during boreal summer (July); however, at the surface, the v5-07-08 OH has an earlier peak in June and also shows a second peak in October, when the v9-01-03 OH shows a decline. The seasonal cycles at higher altitudes are more consistent between the two OH versions. On both annual and seasonal scales, the v5-07-08 fields show lower surface OH above most land regions and NH ocean regions. A similar pattern is observed at higher altitudes (500 hPa), but with smaller and more diffuse differences.

Figure 12a shows the monthly global total column $P(CO)_{CH_4}$ from the coupled and *coupled-origOH* simulation. Using the default v5-07-08 OH fields for the $L(CH_{4Trop})$ and $P(CO)_{CH_4}$ calculations results in a 43 Tg CO yr^{-1} global decrease (≈5% change) relative to the coupled simulation (coupled 913 Tg CO yr^{-1}, *coupled-origOH* 870 Tg CO yr^{-1}), with weaker $P(CO)_{CH_4}$ in the *coupled-origOH* simulation due to lower OH values (Figure S2). The *coupled-origOH* $P(CO)_{CH_4}$ shows weaker production globally between May–September. The weaker $P(CO)_{CH_4}$ is present over land, whereas stronger production is observed over tropical and SH ocean regions (Figure 12b), following the differences in the spatial distribution of the OH fields (Figures S3 and S4).

The same OH field (v9-01-03) was used to calculate L(CO) and P(CO_2) in the coupled and *coupled-origOH* simulation; hence, the P(CO_2) is only impacted by differences in the component of the total CO loss that comes from CO_{CH_4}, which itself is only affected by $P(CO)_{CH_4}$ through L(CH_4). As a result, using the v5-07-08 OH fields for the $L(CH_{4Trop})$ calculation has a smaller impact on P(CO_2). Both the *coupled-origOH* and coupled simulations show similar P(CO_2) budgets but with stronger production in the coupled simulation between June–October (Figure 12e, 1.03 Pg *C* yr^{-1} coupled and 1.02 Pg *C* yr^{-1} in the *coupled-origOH*, ≈1% change). Similar to $P(CO)_{CH_4}$, the *coupled-origOH* shows weaker P(CO_2) everywhere except for tropical and SH ocean regions; however, the differences are more diffuse due to the indirect impact of the OH differences on P(CO_2).

Figure 12c shows the surface mole fractions of the chemical production of CO from CH_4. Using inconsistent OH fields between simulations leads to significant differences in the CO_{CH_4} seasonal cycle. In the *coupled-origOH* simulation, the mole fractions have an inverted seasonal cycle relative to the coupled results, showing a maximum in boreal winter and minimum in boreal summer. The inverted and incorrect seasonal cycle in the *coupled-origOH* simulation is driven by biases in the v5-07-08 OH fields. A detailed discussion of the seasonal cycle difference can be found in Section S2. For CO_{2CO} (Figure 12g), both simulations show a similar seasonal cycle, with slightly higher values in the coupled

simulation due to stronger production. Similar to the total column production, the CO_{CH_4} mole fractions at the surface are highest in the tropical and SH ocean regions in the *coupled-origOH* simulation due to the stronger chemical production. The CO_{2CO} differences are more hemispheric, with lower mole fractions in the NH and higher mole fractions in the SH in the *coupled-origOH* simulation.

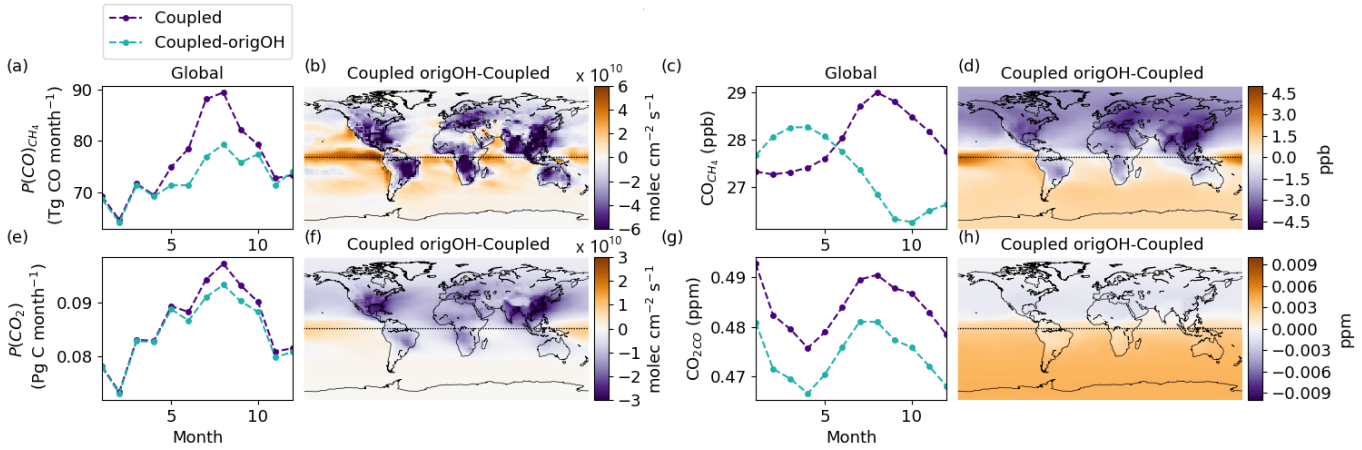

Figure 12. Monthly total atmospheric column CO production from CH_4 (**a**) and CO_2 production from CO (**e**), as well as surface mole fractions of CO_{CH_4} (**c**) and CO_{2CO} (**g**) from the coupled (indigo) and *coupled-origOH* (turquoise) simulation. Subplots (**b**,**f**) show the annual total column production difference between the *coupled-origOH* and coupled simulation, and (**d**,**h**) show the same but for the surface mole fractions of the chemical productions. All of the data are based on year 2006. Note that the CO_2 values are detrended and added to the 2006 growth rate.

We find that inconsistencies in the OH fields in the individual uncoupled simulations can have a significant impact on the production and loss terms, as well as the resulting mole fractions. Using the v5-07-08 OH fields that are currently the default in the v12.1.1 uncoupled CH_4 simulation showed an incorrect seasonal cycle of the CO_{CH_4} mole fractions, and, without the new coupling capability, this bias would not have been identified. By coupling CH_4, CO and CO_2, we therefore increase the consistency between GEOS-Chem simulations of these gases, not only by coupling their chemical production and loss terms but also by removing "hidden" inconsistencies between the individual simulations that arise through the use of different default OH fields.

4. Conclusions

We developed a coupled carbon greenhouse gas simulation in the GEOS-Chem chemical transport model that combines CH_4, CO and CO_2 through their chemical interdependence. The coupling between the three gases comes from the chemical production of CO from CH_4 loss ($P(CO)_{CH_4}$) and the chemical production of CO_2 from the oxidation of CO ($P(CO_2)$). In the uncoupled versions of these simulations that are currently widely used by the GEOS-Chem community, the chemical production calculations were handled offline based on monthly archived fields for specific years from older model versions. Moreover, the uncoupled simulations used inconsistent OH fields between the three gases. The new coupled simulation uses updated and consistent OH fields for all aspects of the simulation. We calculated $P(CO)_{CH_4}$ and $P(CO_2)$ at every model timestep, enabling us to simulate the inter-annual variability of the chemical production fields and their follow-on effects.

Our budget estimates from the coupled simulation agree with known literature values. For the 2006–2017 time period, our coupled results show an increase in $P(CO)_{CH_4}$ with time and a dependence on climate anomalies (such as El Niño Southern Oscillation). We found differences between the coupled and uncoupled simulations ranging from 11–55 Tg CO yr^{-1}, with stronger production in the coupled simulation. Our $P(CO_2)$ from the coupled simulation is weaker than in the uncoupled simulation, with a difference of 0.04–0.09 Pg *C* yr^{-1}.

Comparing the modeled values with three measurement products (TCCON total column measurements, NOAA GGGRN surface measurements and ATom aircraft data) led to (on average) a smaller model–measurement bias using the coupled simulation than using the original uncoupled simulations (except for CO_2 aircraft data); however, the reduced bias from the coupling could potentially be compensating for biases in other emissions fields. For CO, the remaining model–measurement biases in the SH can partially be explained by underestimated biomass burning emissions [10,58,66], especially during the dry season, and underestimated secondary CO production (CH_4 and NMVOC oxidation) [30]. Our coupled simulation suggests stronger P(CO_2) above tropical land regions than simulated previously and that the chemical production of CO_2 in the Amazon was significantly underestimated in previous P(CO_2) studies [15]. South America, Central Africa and northern Australia are characterized by strong biomass burning [67], and our coupled model simulates the P(CO_2) in these regions during the fire season to be stronger than in previous model versions, while the stronger P(CO_2) in regions such as East Asia [68] and North America points to enhanced anthropogenic CO emissions. For CO_2, the inclusion of the missing exchange from air–sea ice interaction could potentially contribute to better modeled values in the polar regions [64]. Our coupled model still excludes the OH feedback [34,50], which may be responsible for persistent biases in the modeled values, especially in regions where chemical production/loss is enhanced.

Our coupled simulation includes two major improvements relative to the default individual carbon gas simulations currently in use by the community: (i) the chemical coupling between species described above and (ii) consistent OH fields used for calculating CH_4 and CO loss. Using a sensitivity simulation, where we use the coupled simulation but retain the original (inconsistent) OH fields, we highlight the importance of using consistent and updated OH fields. We show that the default v5-07-08 OH fields currently used in the uncoupled v12.1.1 CH_4 simulation result in incorrect L(CH_4) and, by extension, $P(CO)_{CH_4}$ values, with an inverted seasonal cycle. In the coupled model, this has flow-on effects for CO and, to a lesser extent, CO_2.

The newly developed coupled simulation enables future investigations of the co-variations of CH_4, CO and CO_2, as well as their interannual variability, that will provide a better understanding of their interactions. We have shown that coupling the three gases improves model consistency, along with our ability to identify source and sink fields that are over- or underestimated in the model. The model–measurement differences are heavily influenced by the existing uncertainties in a variety of carbon gas sources and sinks [10,46,69]. The new coupled simulation paves the way for future improvements, including the inclusion of a CH_4–OH–CO feedback, additional source/sink fields, improvements to the CO yield estimates from CH_4 oxidation and implementation into the GEOS-Chem Adjoint used for inverse modeling, that will further improve our ability to constrain the fluxes of the carbon gases. With updates such as this simulation, we will be able to better highlight and identify the origin of the model–measurement differences and constrain the sources, sinks and budgets of CO_2, CH_4 and CO, crucial for future climate projections and mitigation policies.

Supplementary Materials: The following supporting information can be downloaded at: https://www.mdpi.com/article/10.3390/atmos14050764/s1, Figure S1: Global production of CO from CH_4 (a, d), its loss via OH (b, e) and their difference (c, f) in the coupled (indigo) and *coupled-origOH* (turquoise) simulations at the surface (a–c) and 500 hPa altitude (d–f) for year 2006.; Table S1: GEOS-Chem emission inventories used for both the uncoupled and coupled carbon gas simulations.; Figure S2: Globally averaged OH fields at the surface (a) and at 500 hPa (b) from the v9-01-03 (indigo, used by uncoupled CO and coupled simulation), v8-02-01 (red, uncoupled CO_2) and v5-07-08 (turquoise, uncoupled CH_4 and *coupled-origOH*) full chemistry simulations.; Figure S3: Surface (a–c) and 500 hPa (d–f) yearly averaged global spatial distribution of the OH fields based on the v9-01-03 (a, d) full chemistry simulation and the difference between v5-07-08–v9-01-03 (b, e) and v8-02-01–v9-01-03 (c, f); Figure S4: Surface yearly averaged global spatial distribution of the OH fields based on the v9-01-03 (a, d, g, j) full chemistry simulation and the difference between v5-07-08–v9-01-03 (b, e, h, k) and v8-02-01–v9-01-03 (c, f, i, l) for each season: December–January–February

(DJF, a–c), March–April–May (MAM, d–f), June–July–August (JJA, g–i), September–October–November (SON, j–l).; Figure S5: Annual budgets of the global and regional CO production from CH_4 from the uncoupled (a) and coupled (b) simulation.; Figure S6: Annual budgets of the global and regional CO_2 production from the uncoupled (a) and coupled (b) simulations.; Figure S7: Average December–January–February (DJF) 2006–2017 total column CO chemical production from CH_4 (a), corresponding mole fractions (i.e., CO_{CH_4}) at the surface (b) and at 500 hPa (c) from the coupled simulation along with the difference in each field between the coupled and uncoupled simulation (d–f).; Figure S8: Average March–April–May (MAM) 2006–2017 total column CO chemical production from CH_4 (a), corresponding mole fractions (i.e., CO_{CH_4}) at the surface (b) and at 500 hPa (c) from the coupled simulation along with the difference in each field between the coupled and uncoupled simulation (d–f).; Figure S9: Average June–July–August (JJA) 2006–2017 total column CO chemical production from CH_4 (a), corresponding mole fractions (i.e., CO_{CH_4}) at the surface (b) and at 500 hPa (c) from the coupled simulation along with the difference in each field between the coupled and uncoupled simulation (d–f).; Figure S10: Average September–October–November (SON) 2006–2017 total column CO chemical production from CH_4 (a), corresponding mole fractions (i.e., CO_{CH_4}) at the surface (b) and at 500 hPa (c) from the coupled simulation along with the difference in each field between the coupled and uncoupled simulation (d–f).; Figure S11: Average December–January–February (DJF) 2006–2017 total column CO_2 chemical production from CO (a) and corresponding mole fractions (i.e., CO_{2CO}) at the surface (b) and at 500 hPa (c) from the coupled simulation along with the difference in each field between the coupled and uncoupled simulation (d–f).; Figure S12: Average March–April–May (MAM) 2006–2017 total column CO_2 chemical production from CO (a) and corresponding mole fractions (i.e., CO_{2CO}) at the surface (b) and at 500 hPa (c) from the coupled simulation along with the difference in each field between the coupled and uncoupled simulation (d–f).; Figure S13: Average June–July–August (JJA) 2006–2017 total column CO_2 chemical production from CO (a) and corresponding mole fractions (i.e., CO_{2CO}) at the surface (b) and at 500 hPa (c) from the coupled simulation along with the difference in each field between the coupled and uncoupled simulation (d–f).; Figure S14: Average September–October–November (SON) 2006–2017 total column CO_2 chemical production from CO (a) and corresponding mole fractions (i.e., CO_{2CO}) at the surface (b) and at 500 hPa (c) from the coupled simulation along with the difference in each field between the coupled and uncoupled simulation (d–f).; Figure S15: Modelled CO (red-uncoupled, indigo-coupled) comparison with column measurements (black) at different TCCON sites (top plots), based on monthly average values. Note, the plots show the scaled CO TCCON values (see main text for details). The bottom plots represent the mixing ratios of the CO production from CH_4 from the different simulations. Note, Equation (14) (main text) cannot be directly used when calculating the column-averaged dry-air mole fractions of the chemical terms (i.e., CO_{2CO} and CO_{CH_4}) since the a priori (x_a) represents the profile of the total amount of each gas and has no information about the individual source contributions. The contribution of the a priori profiles is excluded for the calculation of CO_{CH_4}, which is converted to column-averaged dry-air mole fractions according to $c_s = h^T a^T x_m$.; Figure S16: Modelled CO_2 (red-uncoupled, indigo-coupled) comparison with column measurements (black) at different TCCON sites (top plots), based on monthly average values. The detrended values are shown in the middle plots. The bottom plots represent the detrended mixing ratios of the CO_2 production from CO from the different simulations. Note, Equation (14) (main text) cannot be directly used when calculating the column-averaged dry-air mole fractions of the chemical terms (i.e., CO_{2CO} and CO_{CH_4}) since the a priori (x_a) represents the profile of the total amount of each gas and has no information about the individual source contributions. The contribution of the a priori profiles is excluded for the calculation of CO_{2CO}, which is converted to column-averaged dry-air mole fractions according to $c_s = h^T a^T x_m$.; Figure S17: Modelled CO (red-uncoupled, indigo-coupled) comparison with surface measurements (black, top plots), based on monthly average values. The bottom plots represent the mixing ratios of the CO production from CH_4 from the different simulations.; Figure S18: Modelled CO_2 (red-uncoupled, indigo-coupled) comparison with surface measurements (black, top plots), based on monthly average values. The detrended values are shown in the middle plots. The bottom plots represent the detrended mixing ratios of the CO_2 production from CO from the different simulations.; Figure S19: Model-measurement differences for CO (a, b) and CO_2 (c, d) based on simulated values from the uncoupled (a,c) and coupled (b,d) simulations during the four ATom campaigns.; Figure S20: Altitude versus latitude cross-sections of chemically produced *CO* from CH_4 (CO_{CH_4}, a, b, e, f, i, j, m, n) and CO_2 (CO_{2CO}, c, d, g, h, k, l, o, p) mole fractions from the

coupled simulation along with the uncoupled differences relative to the coupled simulation during the four ATom campaigns. References [70–82] are cited in the supplementary materials.

Author Contributions: Conceptualization, B.B., J.A.F., N.M.D. and D.B.A.J.; methodology, B.B., J.A.F., N.M.D. and D.B.A.J.; software, B.B.; validation, B.B.; formal analysis, B.B.; investigation, B.B.; data curation, B.B.; writing—original draft preparation, B.B., J.A.F., N.M.D. and D.B.A.J.; visualization, B.B.; supervision, N.M.D. and J.A.F.; funding acquisition, N.M.D. All authors have read and agreed to the published version of the manuscript.

Funding: This research was funded by the Australian Research Council grant number DE140100178, DP160101598 and FT180100327, Discovery Early Career Researcher (DECRA) University Postgraduate Award from the University of Wollongong, assistance of resources provided at the NCI National Facility systems at the Australian National University through the National Computational Merit Allocation Scheme supported by the Australian government grant number m19 and funding from New Zealand's Ministry of Business, Innovation and Employment through contract number C01X1817.

Institutional Review Board Statement: Not applicable.

Informed Consent Statement: Not applicable.

Data Availability Statement: GEOS-Chem is an open-source model and the coupled simulation is being implemented in an upcoming newer version of GEOS-Chem. The original v12.1.1 model is publicly available at https://doi.org/10.5281/zenodo.2249246 (accessed on 10 March 2023) and the implementation of the coupled simulation and results are available from the authors upon request. TCCON data are publicly available at https://tccondata.org/ (accessed on 10 March 2023). NOAA GGGRN surface data are publicly available at https://www.esrl.noaa.gov/gmd/dv/data/ (accessed on 10 March 2023). ATom data are publicly available at https://doi.org/10.3334/ORNLDAAC/1581. (accessed on 10 March 2023).

Acknowledgments: We thank Clare Paton-Walsh and Sara E. Mikaloff-Fletcher for valuable discussions about this paper. We thank the TCCON PIs and funding agencies for the TCCON measurements. We thank the NOAA ESRL Global Monitoring Laboratory, Boulder, Colorado, USA, for providing the different surface site data. We acknowledge the ATom Team for providing the aircraft data from all four campaigns.

Conflicts of Interest: The authors declare no conflict of interest.

Appendix A

Table A1. Column and surface stations used for the coupled simulation validation. Sites are ordered based on latitude, from highest to lowest.

Station	Latitude	Longitude	Elevation (m)
TCCON sites			
Eureka [1]	80.05° N	86.42° W	610
Ny Alesund [2]	78.90° N	11.89° E	20
Sodankyla [3]	67.37° N	26.63° E	188
Białystok [4]	53.23° N	23.02° E	180
Bremen [5]	53.10° N	8.85° E	27
Karlsruhe [6]	49.10° N	8.43° E	116
Orléans [7]	47.97° N	2.11° E	130
Garmisch [8]	47.48° N	11.06° E	740
Rikubetsu [9]	43.46° N	143.77° E	380
Lamont [10]	36.60° N	97.49° W	320
Anmyeondo [11]	36.54° N	126.33° E	30
Tsukuba [12]	36.05° N	140.12° E	30
Edwards [13]	34.96° N	117.88° W	699
Saga [14]	33.24° N	130.29° E	7
Burgos [15]	18.53° N	120.62° E	35

Table A1. *Cont.*

Station	Latitude	Longitude	Elevation (m)
Manaus [16]	3.21° S	60.60° W	50
Darwin [17]	12.43° S	130.89° E	30
Reunion Island [18]	20.90° S	55.48° E	87
Wollongong [19]	34.41° S	150.88° E	30
Lauder [20]	45.04° S	169.68° E	370
Both TCCON sites and surface [24,25,26]			
Park Falls [21]	45.94° N	90.27° W	440
Izana [22]	28.30° N	16.50° W	2370
Ascension Island [23]	7.91° S	14.33° W	10
Surface sites [24,25,26]			
Alert	82.45° N	62.51° W	185
Summit	72.50° N	38.42° W	3209
Barrow	71.32° N	156.61° W	11
Pallas Sammaltunturi	67.97° N	24.12° E	565
Mace Head	53.33° N	9.89° W	5
Trinidad Head	41.06° N	124.15° W	107
Mt. Waliguan	36.29° N	100.89° E	3810
Assekrem	23.26° N	5.63° E	2710
Mauna Loa	19.53° N	155.58° W	3397
Christmas Island	1.70° N	157.15° W	0
Tutuila	14.25° S	170.56° W	42
Easter Island	27.16° S	109.43° W	47
Cape Grim	40.67° S	144.69° E	94
Baring Head	41.41° S	174.87° E	85
Crozet	46.43° S	51.84° E	197
Palmer Station	64.77° S	64.05° W	10
South Pole	89.98° S	24.80° W	2810

[1] Stronget al. [83] [2] Notholt et al. [84] [3] Kivi et al. [85] [4] Deutscher et al. [86] [5] Notholt et al. [87] [6] Hase et al. [88] [7] Warneke et al. [89] [8] Sussmann and Rettinger [90] [9] Morino et al. [91] [10] Wennberg et al. [92] [11] Goo et al. [93] [12] Morino et al. [94] [13] Iraci et al. [95] [14] Kawakami et al. [96] [15] Morino et al. [97] [16] Dubey et al. [98] [17] Griffith et al. [99] [18] De Mazière et al. [100] [19] Griffith et al. [101] [20] Sherlock et al. [102] [21] Wennberg et al. [103] [22] Blumenstock et al. [104] [23] Feistet al. [105] [24] CO_2: Dlugokencky et al. [53] [25] CH_4: Dlugokencky et al. [53] [26] CO: Petron et al. [54].

References

1. Stocker, T.; Qin, D.; Plattner, G.K.; Tignor, M.; Allen, S.; Boschung, J.; Nauels, A.; Xia, Y.; Bex, V.; Midgley, P. *IPCC, 2013: Climate Change 2013: The Physical Science Basis. Contribution of Working Group I to the Fifth Assessment Report of the Intergovernmental Panel on Climate Change*; Cambridge University Press: Cambridge, UK, 2014.
2. Shindell, D.T.; Faluvegi, G.; Bell, N.; Schmidt, G.A. An emissions-based view of climate forcing by methane and tropospheric ozone. *Geophys. Res. Lett.* **2005**, *32*. [CrossRef]
3. Bousquet, P.; Ciais, P.; Miller, J.; Dlugokencky, E.; Hauglustaine, D.; Prigent, C.; Van der Werf, G.; Peylin, P.; Brunke, E.G.; Carouge, R.; et al. Contribution of anthropogenic and natural sources to atmospheric methane variability. *Nature* **2006**, *443*, 439–443. [CrossRef]
4. Duncan, B.N.; Logan, J.A.; Bey, I.; Megretskaia, I.A.; Yantosca, R.M.; Novelli, P.C.; Jones, N.B.; Rinsland, C.P. Global budget of CO, 1988–1997: Source estimates and validation with a global model. *J. Geophys. Res. Atmos.* **2007**, *112*. [CrossRef]
5. Liu, J.; Bowman, K.W.; Schimel, D.S.; Parazoo, N.C.; Jiang, Z.; Lee, M.; Bloom, A.A.; Wunch, D.; Frankenberg, C.; Sun, Y.; et al. Contrasting carbon cycle responses of the tropical continents to the 2015–2016 El Niño. *Science* **2017**, *358*, eaam5690. [CrossRef]
6. Bloom, A.A.; Bowman, K.W.; Lee, M.; Turner, A.J.; Schroeder, R.; Worden, J.R.; Weidner, R.; McDonald, K.C.; Jacob, D.J. A global wetland methane emissions and uncertainty dataset for atmospheric chemical transport models (WetCHARTs version 1.0). *Geosci. Model Dev.* **2017**, *10*, 2141–2156. [CrossRef]
7. Turner, A.J.; Jacob, D.J.; Wecht, K.J.; Maasakkers, J.D.; Lundgren, E.; Andrews, A.E.; Biraud, S.C.; Boesch, H.; Bowman, K.W.; Deutscher, N.M.; et al. Estimating global and North American methane emissions with high spatial resolution using GOSAT satellite data. *Atmos. Chem. Phys.* **2015**, *15*, 7049–7069. [CrossRef]

8. Wang, J.S.; Logan, J.A.; McElroy, M.B.; Duncan, B.N.; Megretskaia, I.A.; Yantosca, R.M. A 3-D model analysis of the slowdown and interannual variability in the methane growth rate from 1988 to 1997. *Glob. Biogeochem. Cycles* **2004**, *18*. [CrossRef]
9. Messerschmidt, J.; Parazoo, N.; Wunch, D.; Deutscher, N.M.; Roehl, C.; Warneke, T.; Wennberg, P.O. Evaluation of seasonal atmosphere–biosphere exchange estimations with TCCON measurements. *Atmos. Chem. Phys.* **2013**, *13*, 5103–5115. [CrossRef]
10. Bukosa, B.; Deutscher, N.M.; Fisher, J.A.; Kubistin, D.; Paton-Walsh, C.; Griffith, D.W.T. Simultaneous shipborne measurements of CO_2, CH_4 and CO and their application to improving greenhouse-gas flux estimates in Australia. *Atmos. Chem. Phys.* **2019**, *19*, 7055–7072. [CrossRef]
11. Kopacz, M.; Jacob, D.J.; Fisher, J.A.; Logan, J.A.; Zhang, L.; Megretskaia, I.A.; Yantosca, R.M.; Singh, K.; Henze, D.K.; Burrows, J.P.; et al. Global estimates of CO sources with high resolution by adjoint inversion of multiple satellite datasets (MOPITT, AIRS, SCIAMACHY, TES). *Atmos. Chem. Phys.* **2010**, *10*, 855–876. [CrossRef]
12. Palmer, P.I.; Jacob, D.J.; Jones, D.B.A.; Heald, C.L.; Yantosca, R.M.; Logan, J.A.; Sachse, G.W.; Streets, D.G. Inverting for emissions of carbon monoxide from Asia using aircraft observations over the western Pacific. *J. Geophys. Res. Atmos.* **2003**, *108*, 8828. [CrossRef]
13. Enting, I.G.; Mansbridge, J.V. Latitudinal distribution of sources and sinks of CO_2: Results of an inversion study. *Tellus B* **1991**, *43*, 156–170. [CrossRef]
14. Suntharalingam, P.; Randerson, J.T.; Krakauer, N.; Logan, J.A.; Jacob, D.J. Influence of reduced carbon emissions and oxidation on the distribution of atmospheric CO_2: Implications for inversion analyses. *Glob. Biogeochem. Cycles* **2005**, *19*, GB4003. [CrossRef]
15. Nassar, R.; Jones, D.B.A.; Suntharalingam, P.; Chen, J.M.; Andres, R.J.; Wecht, K.J.; Yantosca, R.M.; Kulawik, S.S.; Bowman, K.W.; Worden, J.R.; et al. Modeling global atmospheric CO_2 with improved emission inventories and CO_2 production from the oxidation of other carbon species. *Geosci. Model Dev.* **2010**, *3*, 689–716. [CrossRef]
16. Wecht, K.J.; Jacob, D.J.; Frankenberg, C.; Jiang, Z.; Blake, D.R. Mapping of North American methane emissions with high spatial resolution by inversion of SCIAMACHY satellite data. *J. Geophys. Res. Atmos.* **2014**, *119*, 7741–7756. [CrossRef]
17. Fisher, J.A.; Murray, L.T.; Jones, D.B.A.; Deutscher, N.M. Improved method for linear carbon monoxide simulation and source attribution in atmospheric chemistry models illustrated using GEOS-Chem v9. *Geosci. Model Dev. Discuss.* **2017**, *2017*, 4129–4144. [CrossRef]
18. Jacob, D.J. *Introduction to Atmospheric Chemistry*; Princeton University Press: Princeton, NJ, USA, 1999.
19. Isaksen, I.S.; Hov, Ø. Calculation of trends in the tropospheric concentration of O_3, OH, CO, CH_4 and NO_x. *Tellus B* **1987**, *39B*, 271–285. [CrossRef]
20. Folberth, G.; Hauglustaine, D.A.; Ciais, P.; Lathière, J. On the role of atmospheric chemistry in the global CO_2 budget. *Geophys. Res. Lett.* **2005**, *32*, L08801. [CrossRef]
21. Logan, J.A.; Prather, M.J.; Wofsy, S.C.; McElroy, M.B. Tropospheric chemistry: A global perspective. *J. Geophys. Res. Ocean.* **1981**, *86*, 7210–7254. [CrossRef]
22. Tie, X.; Jim Kao, C.Y.; Mroz, E. Net yield of OH, CO, and O_3 from the oxidation of atmospheric methane. *Atmos. Environ. Part A Gen. Top.* **1992**, *26*, 125–136. [CrossRef]
23. Manning, M.R.; Brenninkmeijer, C.A.M.; Allan, W. Atmospheric carbon monoxide budget of the southern hemisphere: Implications of 13C/12C measurements. *J. Geophys. Res. Atmos.* **1997**, *102*, 10673–10682. [CrossRef]
24. Novelli, P.C.; Lang, P.M.; Masarie, K.A.; Hurst, D.F.; Myers, R.; Elkins, J.W. Molecular hydrogen in the troposphere: Global distribution and budget. *J. Geophys. Res. Atmos.* **1999**, *104*, 30427–30444. [CrossRef]
25. Bergamaschi, P.; Hein, R.; Brenninkmeijer, C.A.M.; Crutzen, P.J. Inverse modeling of the global CO cycle: 2. Inversion of 13C/12C and 18O/16O isotope ratios. *J. Geophys. Res. Atmos.* **2000**, *105*, 1929–1945. [CrossRef]
26. Franco, B.; Blumenstock, T.; Cho, C.; Clarisse, L.; Clerbaux, C.; Coheur, P.F.; De Mazière, M.; De Smedt, I.; Dorn, H.P.; Emmerichs, T.; et al. Ubiquitous atmospheric production of organic acids mediated by cloud droplets. *Nature* **2021**, *593*, 233–237. [CrossRef] [PubMed]
27. Holloway, T.; Levy II, H.; Kasibhatla, P. Global distribution of carbon monoxide. *J. Geophys. Res. Atmos.* **2000**, *105*, 12123–12147. [CrossRef]
28. Arellano, A.F., Jr.; Hess, P.G. Sensitivity of top-down estimates of CO sources to GCTM transport. *Geophys. Res. Lett.* **2006**, *33*, L21807. [CrossRef]
29. Stein, O.; Schultz, M.G.; Bouarar, I.; Clark, H.; Huijnen, V.; Gaudel, A.; George, M.; Clerbaux, C. On the wintertime low bias of Northern Hemisphere carbon monoxide found in global model simulations. *Atmos. Chem. Phys.* **2014**, *14*, 9295–9316. [CrossRef]
30. Zeng, G.; Williams, J.E.; Fisher, J.A.; Emmons, L.K.; Jones, N.B.; Morgenstern, O.; Robinson, J.; Smale, D.; Paton-Walsh, C.; Griffith, D.W.T. Multi-model simulation of CO and HCHO in the Southern Hemisphere: Comparison with observations and impact of biogenic emissions. *Atmos. Chem. Phys.* **2015**, *15*, 7217–7245. [CrossRef]
31. Pétron, G.; Granier, C.; Khattatov, B.; Yudin, V.; Lamarque, J.F.; Emmons, L.; Gille, J.; Edwards, D.P. Monthly CO surface sources inventory based on the 2000–2001 MOPITT satellite data. *Geophys. Res. Lett.* **2004**, *31*, L21107. [CrossRef]
32. Le Quéré, C.; Andrew, R.M.; Friedlingstein, P.; Sitch, S.; Hauck, J.; Pongratz, J.; Pickers, P.A.; Korsbakken, J.I.; Peters, G.P.; Canadell, J.G.; et al. Global Carbon Budget 2018. *Earth Syst. Sci. Data* **2018**, *10*, 2141–2194. [CrossRef]
33. Ciais, P.; Borges, A.V.; Abril, G.; Meybeck, M.; Folberth, G.; Hauglustaine, D.; Janssens, I.A. The impact of lateral carbon fluxes on the European carbon balance. *Biogeosciences* **2008**, *5*, 1259–1271. [CrossRef]

34. Elshorbany, Y.F.; Duncan, B.N.; Strode, S.A.; Wang, J.S.; Kouatchou, J. The description and validation of the computationally Efficient CH_4–CO–OH (ECCOHv1.01) chemistry module for 3-D model applications. *Geosci. Model Dev.* **2016**, *9*, 799–822. [CrossRef]
35. Pison, I.; Bousquet, P.; Chevallier, F.; Szopa, S.; Hauglustaine, D. Multi-species inversion of CH_4, CO and H_2 emissions from surface measurements. *Atmos. Chem. Phys.* **2009**, *9*, 5281–5297. [CrossRef]
36. Wang, H.; Jacob, D.J.; Kopacz, M.; Jones, D.B.A.; Suntharalingam, P.; Fisher, J.A.; Nassar, R.; Pawson, S.; Nielsen, J.E. Error correlation between CO_2 and CO as constraint for CO_2 flux inversions using satellite data. *Atmos. Chem. Phys.* **2009**, *9*, 7313–7323. [CrossRef]
37. Pandey, S.; Houweling, S.; Krol, M.; Aben, I.; Röckmann, T. On the use of satellite-derived CH_4 : CO_2 columns in a joint inversion of CH_4 and CO_2 fluxes. *Atmos. Chem. Phys.* **2015**, *15*, 8615–8629. [CrossRef]
38. Nassar, R.; Napier-Linton, L.; Gurney, K.R.; Andres, R.J.; Oda, T.; Vogel, F.R.; Deng, F. Improving the temporal and spatial distribution of CO_2 emissions from global fossil fuel emission data sets. *J. Geophys. Res. Atmos.* **2013**, *118*, 917–933. [CrossRef]
39. Maasakkers, J.D.; Jacob, D.J.; Sulprizio, M.P.; Scarpelli, T.R.; Nesser, H.; Sheng, J.X.; Zhang, Y.; Hersher, M.; Bloom, A.A.; Bowman, K.W.; et al. Global distribution of methane emissions, emission trends, and OH concentrations and trends inferred from an inversion of GOSAT satellite data for 2010–2015. *Atmos. Chem. Phys.* **2019**, *19*, 7859–7881. [CrossRef]
40. Considine, D.B.; Logan, J.A.; Olsen, M.A. Evaluation of near-tropopause ozone distributions in the Global Modeling Initiative combined stratosphere/troposphere model with ozonesonde data. *Atmos. Chem. Phys.* **2008**, *8*, 2365–2385. [CrossRef]
41. Allen, D.; Pickering, K.; Duncan, B.; Damon, M. Impact of lightning NO emissions on North American photochemistry as determined using the Global Modeling Initiative (GMI) model. *J. Geophys. Res. Atmos.* **2010**, *115*, D22301. [CrossRef]
42. Murray, L.T.; Jacob, D.J.; Logan, J.A.; Hudman, R.C.; Koshak, W.J. Optimized regional and interannual variability of lightning in a global chemical transport model constrained by LIS/OTD satellite data. *J. Geophys. Res. Atmos.* **2012**, *117*, D20307. [CrossRef]
43. Burkholder, J.B.; Sander, S.P.; Abbatt, J.; Barker, J.R.; Huie, R.E.; Kolb, C.E.; Kurylo, M.J.; Orkin, V.L.; Wilmouth, D.M.; Wine, P.H. *Chemical Kinetics and Photochemical Data for Use in Atmospheric Studies, Evaluation No. 18*; JPL Publication 15-10; Jet Propulsion Laboratory: Pasadena, TX, USA, 2015.
44. Park, R.J.; Jacob, D.J.; Field, B.D.; Yantosca, R.M.; Chin, M. Natural and transboundary pollution influences on sulfate-nitrate-ammonium aerosols in the United States: Implications for policy. *J. Geophys. Res. Atmos.* **2004**, *109*, D15204. [CrossRef]
45. Darmenov, A.; da Silva, A. The quick fire emissions dataset (QFED)–documentation of versions 2.1, 2.2 and 2.4. *NASA Technical Report Series on Global Modeling and Data Assimilation*; NASA TM-2013-104606; NASA: Washington, DC, USA, 2015; Volume 32, p. 183.
46. Dlugokencky, E.J.; Nisbet, E.G.; Fisher, R.; Lowry, D. Global atmospheric methane: Budget, changes and dangers. *Philos. Trans. R. Soc. A Math. Phys. Eng. Sci.* **2011**, *369*, 2058–2072. [CrossRef] [PubMed]
47. Hodson, E.L.; Poulter, B.; Zimmermann, N.E.; Prigent, C.; Kaplan, J.O. The El Niño–Southern Oscillation and wetland methane interannual variability. *Geophys. Res. Lett.* **2011**, *38*, L08810. [CrossRef]
48. Schaefer, H.; Smale, D.; Nichol, S.E.; Bromley, T.M.; Brailsford, G.W.; Martin, R.J.; Moss, R.; Englund Michel, S.; White, J.W.C. Limited impact of El Niño–Southern Oscillation on variability and growth rate of atmospheric methane. *Biogeosciences* **2018**, *15*, 6371–6386. [CrossRef]
49. Rowlinson, M.J.; Rap, A.; Arnold, S.R.; Pope, R.J.; Chipperfield, M.P.; McNorton, J.; Forster, P.; Gordon, H.; Pringle, K.J.; Feng, W.; et al. Impact of El Niño–Southern Oscillation on the interannual variability of methane and tropospheric ozone. *Atmos. Chem. Phys.* **2019**, *19*, 8669–8686. [CrossRef]
50. Holmes, C.D. Methane Feedback on Atmospheric Chemistry: Methods, Models, and Mechanisms. *J. Adv. Model. Earth Syst.* **2018**, *10*, 1087–1099. [CrossRef]
51. Edwards, D.P.; Emmons, L.K.; Gille, J.C.; Chu, A.; Attié, J.L.; Giglio, L.; Wood, S.W.; Haywood, J.; Deeter, M.N.; Massie, S.T.; et al. Satellite-observed pollution from Southern Hemisphere biomass burning. *J. Geophys. Res. Atmos.* **2006**, *111*, D14312. [CrossRef]
52. Wunch, D.; Toon, G.C.; Blavier, J.F.L.; Washenfelder, R.A.; Notholt, J.; Connor, B.J.; Griffith, D.W.T.; Sherlock, V.; Wennberg, P.O. The Total Carbon Column Observing Network. *Philos. Trans. R. Soc. A Math. Phys. Eng. Sci.* **2011**, *369*, 2087–2112. [CrossRef]
53. Dlugokencky, E.J.; Mund, J.W.; Crotwell, A.M.; Crotwell, M.J.; Thoning, K.W. Atmospheric Carbon Dioxide Dry Air Mole Fractions from the NOAA GML Carbon Cycle Cooperative Global Air Sampling Network, 1968–2019. Version: 2020-07. *arXiv* **2020**, arXiv:2012.00839. https://doi.org/10.15138/wkgj-f215.
54. Petron, G.; Crotwell, A.M.; Crotwell, M.J.; Dlugokencky, E.J.; Madronich, M.; Moglia, E.; Neff, D.; Wolter, S.; Mund, J. Atmospheric Carbon Monoxide Dry Air Mole Fractions from the NOAA GML Carbon Cycle Cooperative Global Air Sampling Network, 1988–2020. Version: 2020-08. 2020. Available online: https://gml.noaa.gov/ccgg/arc/?id=132 (accessed on 10 March 2023).
55. Wofsy, S.; Afshar, S.; Allen, H.; Apel, E.; Asher, E.; Barletta, B.; Bent, J.; Bian, H.; Biggs, B.; Blake, D.; et al. ATom: Merged Atmospheric Chemistry, Trace Gases, and Aerosols. *ORNL DAAC* **2018**. [CrossRef]
56. Wunch, D.; Toon, G.C.; Wennberg, P.O.; Wofsy, S.C.; Stephens, B.B.; Fischer, M.L.; Uchino, O.; Abshire, J.B.; Bernath, P.; Biraud, S.C.; et al. Calibration of the Total Carbon Column Observing Network using aircraft profile data. *Atmos. Meas. Tech.* **2010**, *3*, 1351–1362. [CrossRef]
57. Deutscher, N.M.; Sherlock, V.; Mikaloff Fletcher, S.E.; Griffith, D.W.T.; Notholt, J.; Macatangay, R.; Connor, B.J.; Robinson, J.; Shiona, H.; Velazco, V.A.; et al. Drivers of column-average CO_2 variability at Southern Hemispheric Total Carbon Column Observing Network sites. *Atmos. Chem. Phys.* **2014**, *14*, 9883–9901. [CrossRef]

58. Té, Y.; Jeseck, P.; Franco, B.; Mahieu, E.; Jones, N.; Paton-Walsh, C.; Griffith, D.W.T.; Buchholz, R.R.; Hadji-Lazaro, J.; Hurtmans, D.; et al. Seasonal variability of surface and column carbon monoxide over the megacity Paris, high-altitude Jungfraujoch and Southern Hemispheric Wollongong stations. *Atmos. Chem. Phys.* **2016**, *16*, 10911–10925. [CrossRef]
59. Hedelius, J.K.; He, T.L.; Jones, D.B.A.; Baier, B.C.; Buchholz, R.R.; De Mazière, M.; Deutscher, N.M.; Dubey, M.K.; Feist, D.G.; Griffith, D.W.T.; et al. Evaluation of MOPITT Version 7 joint TIR–NIR X_{CO} retrievals with TCCON. *Atmos. Meas. Tech.* **2019**, *12*, 5547–5572. [CrossRef]
60. Zhou, M.; Langerock, B.; Vigouroux, C.; Sha, M.K.; Hermans, C.; Metzger, J.M.; Chen, H.; Ramonet, M.; Kivi, R.; Heikkinen, P.; et al. TCCON and NDACC X_CO measurements: Difference, discussion and application. *Atmos. Meas. Tech.* **2019**, *12*, 5979–5995. [CrossRef]
61. Schuh, A.E.; Jacobson, A.R.; Basu, S.; Weir, B.; Baker, D.; Bowman, K.; Chevallier, F.; Crowell, S.; Davis, K.J.; Deng, F.; et al. Quantifying the impact of atmospheric transport uncertainty on CO2 surface flux estimates. *Glob. Biogeochem. Cycles* **2019**, *33*, 484–500. [CrossRef] [PubMed]
62. Schuh, A.E.; Byrne, B.; Jacobson, A.R.; Crowell, S.M.; Deng, F.; Baker, D.F.; Johnson, M.S.; Philip, S.; Weir, B. On the role of atmospheric model transport uncertainty in estimating the Chinese land carbon sink. *Nature* **2022**, *603*, E13–E14. [CrossRef]
63. Stanevich, I.; Jones, D.B.A.; Strong, K.; Parker, R.J.; Boesch, H.; Wunch, D.; Notholt, J.; Petri, C.; Warneke, T.; Sussmann, R.; et al. Characterizing model errors in chemical transport modeling of methane: Impact of model resolution in versions v9-02 of GEOS-Chem and v35j of its adjoint model. *Geosci. Model Dev.* **2020**, *13*, 3839–3862. [CrossRef]
64. Graham, K.A.; Holmes, C.D.; Friedrich, G.; Rauschenberg, C.D.; Williams, C.R.; Bottenheim, J.W.; Chavez, F.P.; Halfacre, J.W.; Perovich, D.K.; Shepson, P.B.; et al. Variability of Atmospheric CO_2 over the Arctic Ocean: Insights from the O-Buoy Chemical Observing Network. *J. Geophys. Res. Atmos.* **2023**, *128*, e2022JD036437. [CrossRef]
65. Søgaard, D.H.; Thomas, D.N.; Rysgaard, S.; Glud, R.N.; Norman, L.; Kaartokallio, H.; Juul-Pedersen, T.; Geilfus, N.X. The relative contributions of biological and abiotic processes to carbon dynamics in subarctic sea ice. *Polar Biol.* **2013**, *36*, 1761–1777. [CrossRef]
66. Desservettaz, M.J.; Fisher, J.A.; Luhar, A.K.; Woodhouse, M.T.; Bukosa, B.; Buchholz, R.R.; Wiedinmyer, C.; Griffith, D.W.T.; Krummel, P.B.; Jones, N.B.; et al. Australian Fire Emissions of Carbon Monoxide Estimated by Global Biomass Burning Inventories: Variability and Observational Constraints. *J. Geophys. Res. Atmos.* **2022**, *127*, e2021JD035925. [CrossRef]
67. Su, M.; Shi, Y.; Yang, Y.; Guo, W. Impacts of different biomass burning emission inventories: Simulations of atmospheric CO_2 concentrations based on GEOS-Chem. *Sci. Total Environ.* **2023**, *876*, 162825. [CrossRef] [PubMed]
68. Gaubert, B.; Emmons, L.K.; Raeder, K.; Tilmes, S.; Miyazaki, K.; Arellano, A.F., Jr.; Elguindi, N.; Granier, C.; Tang, W.; Barré, J.; et al. Correcting model biases of CO in East Asia: Impact on oxidant distributions during KORUS-AQ. *Atmos. Chem. Phys.* **2020**, *20*, 14617–14647. [CrossRef] [PubMed]
69. Bastos, A.; O'Sullivan, M.; Ciais, P.; Makowski, D.; Sitch, S.; Friedlingstein, P.; Chevallier, F.; Rödenbeck, C.; Pongratz, J.; Luijkx, I.T.; et al. Sources of Uncertainty in Regional and Global Terrestrial CO_2 Exchange Estimates. *Glob. Biogeochem. Cycles* **2020**, *34*, e2019GB006393. [CrossRef]
70. Baker, D.F.; Law, R.M.; Gurney, K.R.; Rayner, P.; Peylin, P.; Denning, A.S.; Bousquet, P.; Bruhwiler, L.; Chen, Y.-H.; Ciais, P.; et al. TransCom 3 inversion intercomparison: Impact of transport model errors on the interannual variability of regional CO_2 fluxes, 1988–2003. *Glob. Biogeochem.* **2006**, *20*. [CrossRef]
71. Fung, I.; John, J.; Lerner, J.; Matthews, E.; Prather, M.; Steele, L.P.; Fraser, P.J. Three-dimensional model synthesis of the global methane cycle. *J. Geophys. Res. Atmos.* **1991**, *96*, 13033–13065., 1991. [CrossRef]
72. Kuhns, H.; Knipping, E.M.; Vukovich, J.M. Development of a United States–Mexico emissions inventory for the big bend regional aerosol and visibility observational (BRAVO) study. *J. Air Waste Manag. Assoc.* **2005**, *55*, 677–692. [CrossRef]
73. Lee, C.; Martin, R.V.; van Donkelaar, A.; Lee, H.; Dickerson, R.R.; Hains, J.C.; Krotkov, N.; Richter, A.; Vinnikov, K.; Schwab, J.J. SO_2 emissions and lifetimes: Estimates from inverse modeling using in situ and global, space-based (SCIAMACHY and OMI) 60 observations. *J. Geophys. Res. Atmos.* **2011**, *116*. [CrossRef]
74. Li, M.; Zhang, Q.; Kurokawa, J.-I.; Woo, J.-H.; He, K.; Lu, Z.; Ohara, T.; Song, Y.; Streets, D.G.; Carmichael, G.R.; et al. MIX: A mosaic Asian anthropogenic emission inventory under the international collaboration framework of the MICS-Asia and HTAP. *Atmos. Chem. Phys.* **2017**, *17*, 935–963. 935-2017. [CrossRef]
75. Maasakkers, J.D.; Jacob, D.J.; Sulprizio, M.P.; Turner, A.J.; Weitz, M.; Wirth, T.; Hight, C.; DeFigueiredo, M.; Desai, M.; Schmeltz, R.; et al. Gridded national inventory of US methane emissions. *Environ. Sci. Technol.* **2016**, *50*, 13123–13133. [CrossRef]
76. Oda, T.; Maksyutov, S. A very high-resolution (1 km × 1 km) global fossil fuel CO_2 emission inventory derived using a point source database and satellite observations of nighttime lights. *Atmos. Chem. Phys.* **2011**, *11*, 543–556. 543-2011. [CrossRef]
77. Sheng, J.-X.; Jacob, D.J.; Maasakkers, J.D.; Sulprizio, M.P.; Zavala-Araiza, D.; Hamburg, S.P. A high-resolution (0.1 × 0.1) inventory of methane emissions from Canadian and Mexican oil and gas systems. *Atmos. Environ.* **2017**, *158*, 211–215. [CrossRef]
78. Stettler, M.; Eastham, S.; Barrett, S. Air quality and public health impacts of UK airports. Part I: Emissions. *Atmos. Environ.* **2011**, *45*, 5415–5424. [CrossRef]
79. Takahashi, T.; Sutherl, S.C.; Wanninkhof, R.; Sweeney, C.; Feely, R.A.; Chipman, D.W.; Hales, B.; Friederich, G.; Chavez, F.; Sabine, C.; et al. Climatological mean and decadal change in surface ocean pCO_2, and net sea–air CO_2 flux over the global oceans. *Deep. Sea 85 Res. Part II Top. Stud. Oceanogr.* **2009**, *56*, 554–577. [CrossRef]

80. Van Donkelaar, A.; Martin, R.V.; Pasch, A.N.; Szykman, J.J.; Zhang, L.; Wang, Y.X.; Chen, D. Improving the accuracy of daily satellite-derived ground-level fine aerosol concentration estimates for North America. *Environ. Sci. Technol.* **2012**, *46*, 11971–11978. [CrossRef] [PubMed]
81. Vestreng, V.; Mareckova, K.; Kakareka, S.; Malchykhina, A.; Kukharchyk, T. Inventory Review 2007. In *Emission Data Reported to LRTAP Convention and NEC Directive, MSC-W Technical Report 1/07*; The Norwegian Meteorological Institute: Oslo, Norway, 2007.
82. Yevich, R.; Logan, J.A. An assessment of biofuel use and burning of agricultural waste in the developing world. *Glob. Biogeochem.* **2003**, *17*. [CrossRef]
83. Strong, K.; Roche, S.; Franklin, J.; Mendonca, J.; Lutsch, E.; Weaver, D.; Fogal, P.; Drummond, J.; Batchelor, R.; Lindenmaier, R. TCCON Data from Eureka (CA), Release GGG2014R3. TCCON Data Archive, Hosted by CaltechDATA. 2019. Available online: https://data.caltech.edu/records/m5vq1-3ga50 (accessed on 10 March 2023).
84. Notholt, J.; Schrems, O.; Warneke, T.; Deutscher, N.M.; Weinzierl, C.; Palm, M.; Buschmann, M. TCCON Data from Ny Ålesund, Spitsbergen (NO), Release GGG2014R1. TCCON Data Archive, Hosted by CaltechDATA. 2019. Available online: https://data.caltech.edu/records/vztb0-vsv44 (accessed on 10 March 2023).
85. Kivi, R.; Heikkinen, P.; Kyrö, E. TCCON Data from Sodankyla (FI), Release GGG2014R0. TCCON Data Archive, Hosted by CaltechDATA. 2014. Available online: https://data.caltech.edu/records/n2823-2yt07 (accessed on 10 March 2023).
86. Deutscher, N.M.; Notholt, J.; Messerschmidt, J.; Weinzierl, C.; Warneke, T.; Petri, C.; Grupe, P.; Katrynski, K. TCCON Data from Bialystok (PL), Release GGG2014R2. TCCON Data Archive, Hosted by CaltechDATA. 2015. Available online: https://data.caltech.edu/records/0cjh6-71m74 (accessed on 10 March 2023).
87. Notholt, J.; Petri, C.; Warneke, T.; Deutscher, N.M.; Buschmann, M.; Weinzierl, C.; Macatangay, R.; Grupe, P. TCCON Data from Bremen (DE), Release GGG2014R1. TCCON Data Archive, Hosted by CaltechDATA. 2019. Available online: https://data.caltech.edu/records/4hszb-99q28 (accessed on 10 March 2023).
88. Hase, F.; Blumenstock, T.; Dohe, S.; Gross, J.; Kiel, M. TCCON Data from Karlsruhe (DE), Release GGG2014R1. TCCON Data Archive, Hosted by CaltechDATA. 2015. Available online: https://data.caltech.edu/records/nhdv7-yfv69 (accessed on 10 March 2023).
89. Warneke, T.; Messerschmidt, J.; Notholt, J.; Weinzierl, C.; Deutscher, N.M.; Petri, C.; Grupe, P.; Vuillemin, C.; Truong, F.; Schmidt, M.; et al. TCCON Data from Orléans (FR), Release GGG2014R0. TCCON Data Archive, Hosted by CaltechDATA. 2014. Available online: https://data.caltech.edu/records/0n6jg-56q50 (accessed on 10 March 2023).
90. Sussmann, R.; Rettinger, M. TCCON Data from Garmisch (DE), Release GGG2014R2. TCCON Data Archive, Hosted by CaltechDATA. 2018. Available online: https://data.caltech.edu/records/7jdn6-vtg92 (accessed on 10 March 2023).
91. Morino, I.; Yokozeki, N.; Matzuzaki, T.; Horikawa, M. TCCON Data from Rikubetsu (JP), Release GGG2014R2. TCCON Data Archive, Hosted by CaltechDATA. 2018. Available online: https://data.caltech.edu/records/8db2k-rcp69 (accessed on 10 March 2023).
92. Wennberg, P.O.; Wunch, D.; Roehl, C.; Blavier, J.F.; Toon, G.C.; Allen, N.; Dowell, P.; Teske, K.; Martin, C.; Martin, J. TCCON Data from Lamont (US), Release GGG2014R1. TCCON Data Archive, Hosted by CaltechDATA. 2016. Available online: https://data.caltech.edu/records/cghqs-qp027 (accessed on 10 March 2023).
93. Goo, T.Y.; Oh, Y.S.; Velazco, V.A. TCCON Data from Anmeyondo (KR), Release GGG2014R0. TCCON Data Archive, Hosted by CaltechDATA. 2014. Available online: https://data.caltech.edu/records/dq9b4-19g61 (accessed on 10 March 2023).
94. Morino, I.; Matsuzaki, T.; Shishime, A. TCCON Data from Tsukuba (JP), 125HR, Release GGG2014R2. TCCON Data Archive, Hosted by CaltechDATA. 2018. Available online: https://data.caltech.edu/records/jgz9c-bwz67 (accessed on 10 March 2023).
95. Iraci, L.T.; Podolske, J.; Hillyard, P.W.; Roehl, C.; Wennberg, P.O.; Blavier, J.F.; Allen, N.; Wunch, D.; Osterman, G.B.; Albertson, R. TCCON Data from Edwards (US), Release GGG2014R1. TCCON Data Archive, Hosted by CaltechDATA. 2016. Available online: https://data.caltech.edu/records/2ssse-s7s41 (accessed on 10 March 2023).
96. Kawakami, S.; Ohyama, H.; Arai, K.; Okumura, H.; Taura, C.; Fukamachi, T.; Sakashita, M. TCCON Data from Saga (JP), Release GGG2014R0. TCCON Data Archive, Hosted by CaltechDATA. 2014. Available online: https://data.caltech.edu/records/q5ch6-1yp60 (accessed on 10 March 2023).
97. Morino, I.; Velazco, V.A.; Akihiro, H.; Osamu, U.; Griffith, D.W.T. TCCON Data from Burgos, Ilocos Norte (PH), Release GGG2014.R0. TCCON Data Archive, Hosted by CaltechDATA. 2018. Available online: https://data.caltech.edu/records/s3x4h-5pv98 (accessed on 10 March 2023).
98. Dubey, M.; Henderson, B.; Green, D.; Butterfield, Z.; Keppel-Aleks, G.; Allen, N.; Blavier, J.F.; Roehl, C.; Wunch, D.; Lindenmaier, R. TCCON Data from Manaus (BR), Release GGG2014R0. TCCON Data Archive, Hosted by CaltechDATA. 2014. Available online: https://data.caltech.edu/records/8pa5g-57r83 (accessed on 10 March 2023).
99. Griffith, D.W.; Deutscher, N.M.; Velazco, V.A.; Wennberg, P.O.; Yavin, Y.; Aleks, G.K.; Washenfelder, R.a.; Toon, G.C.; Blavier, J.F.; Murphy, C.; et al. TCCON Data from Darwin (AU), Release GGG2014R0. TCCON Data Archive, Hosted by CaltechDATA. 2014. Available online: https://data.caltech.edu/records/zmpsc-0ym23 (accessed on 10 March 2023).
100. De Mazière, M.; Sha, M.K.; Desmet, F.; Hermans, C.; Scolas, F.; Kumps, N.; Metzger, J.M.; Duflot, V.; Cammas, J.P. TCCON Data from Reunion Island (RE), Release GGG2014R0. TCCON Data Archive, Hosted by CaltechDATA. 2017. Available online: https://data.caltech.edu/records/k7c8c-6e426 (accessed on 10 March 2023).

101. Griffith, D.W.; Velazco, V.A.; Deutscher, N.M.; Murphy, C.; Jones, N.; Wilson, S.; Macatangay, R.; Kettlewell, G.; Buchholz, R.R.; Riggenbach, M. TCCON Data from Wollongong (AU), Release GGG2014R0. TCCON Data Archive, hosted by CaltechDATA. 2014. Available online: https://data.caltech.edu/records/aqkee-99p67 (accessed on 10 March 2023).
102. Sherlock, V.; Connor, B.J.; Robinson, J.; Shiona, H.; Smale, D.; Pollard, D. TCCON Data from Lauder (NZ), 125HR, Release GGG2014R0. TCCON Data Archive, Hosted by CaltechDATA. 2014. Available online: https://data.caltech.edu/records/2djsk-mpm66 (accessed on 10 March 2023).
103. Wennberg, P.O.; Roehl, C.; Wunch, D.; Toon, G.C.; Blavier, J.F.; Washenfelder, R.a.; Keppel-Aleks, G.; Allen, N.; Ayers, J. TCCON Data from Park Falls (US), Release GGG2014R1. TCCON Data Archive, Hosted by CaltechDATA. 2017. Available online: https://data.caltech.edu/records/ye7gn-2sc61 (accessed on 10 March 2023).
104. Blumenstock, T.; Hase, f.; Schneider, M.; Garcia, O.E.; Sepulveda, E. TCCON Data from Izana (ES), Release GGG2014R1. TCCON Data Archive, Hosted by CaltechDATA. 2017. Available online: https://data.caltech.edu/records/qf1ya-jjy76 (accessed on 10 March 2023).
105. Feist, D.G.; Arnold, S.G.; John, N.; Geibel, M.C. TCCON Data from Ascension Island (SH), Release GGG2014R0. TCCON Data Archive, Hosted by CaltechDATA. 2014. Available online: https://data.caltech.edu/records/rh1kp-b6c90 (accessed on 10 March 2023).